

# Climatological distribution of dissolved inorganic nutrients in the Western Mediterranean Sea (1981-2017)

Malek Belgacem<sup>1,2</sup>, Katrin Schroeder<sup>1</sup>, Alexander Barth<sup>3</sup>, Charles Troupin<sup>3</sup>, Bruno Pavoni<sup>2</sup>, Jacopo Chiggiato<sup>1</sup>, Patrick Rambault<sup>4</sup>, Nicole Garcia<sup>4</sup>,

<sup>1</sup>CNR-ISMAR, Arsenale Tesa 104, Castello 2737/F, 30122 Venezia, Italy

<sup>2</sup>Dipartimento di Scienze Ambientali Informatica e Statistica, DAIS, Università Ca' Foscari Venezia, Campus Scientifico Mestre, Italy

<sup>3</sup>GeoHydrodynamics and Environment Research, GHER, Freshwater and Oceanic sCiences Unit of reSearch (FOCUS), -University of Liège, Quartier Agora, Allée du 6-Août, 17, Sart Tilman, 4000 Liège 1, Belgium

<sup>4</sup>Aix Marseille Université, CNRS/INSU, Université de Toulon, IRD, Mediterranean Institute of Oceanography (MIO) UM 110, 13288, Marseille, France

Correspondence: Malek Belgacem ([malek.belgacem@ve.ismar.cnr.it](mailto:malek.belgacem@ve.ismar.cnr.it))

## Abstract

The Western MEDiterranean Sea BioGeochemical Climatology (BGC-WMED) presented here is a product derived from quality controlled in situ observations. Annual mean gridded nutrient fields for the period 1981-2017, and its sub-periods 1981-2004 and 2005-2017, on a horizontal  $1/4^\circ \times 1/4^\circ$  grid have been produced. The biogeochemical climatology is built on 19 depth levels and for the dissolved inorganic nutrients nitrate, phosphate and orthosilicate. To generate smooth and homogeneous interpolated fields, the method of the Variational Inverse Model (VIM) was applied. A sensitivity analysis was carried out to assess the comparability of the data product with the observational data. The BGC-WMED has then been compared to other available data products, i.e. the medBFM biogeochemical reanalysis of the Mediterranean Sea and the World Ocean Atlas 2018 (WOA18) (its biogeochemical part). The new product reproduces common features with more detailed patterns and agrees with previous records. This suggests a good reference to the region and to the scientific community for the ~~The BGC-WMED product supports the~~ understanding of inorganic nutrient variability in the western Mediterranean Sea, in space and in time, but our new climatology can also can also be used to validate numerical simulations making it a reference data product.

**Keywords:** ~~western~~-Western Mediterranean Sea, climatology, inorganic nutrients, in situ observations.

Formatted: Font: (Default) Times New Roman, 12 pt, Complex Script Font: Times New Roman, 12 pt, Not

Formatted: Font: (Default) Times New Roman, 12 pt, Bold, Complex Script Font: Times New Roman, 12 pt

Formatted: Font: (Default) Times New Roman, 12 pt, Complex Script Font: Times New Roman, 12 pt, Not

Formatted: Font: (Default) Times New Roman, 12 pt, Bold, Complex Script Font: Times New Roman, 12 pt

Formatted: Font: (Default) Times New Roman, 12 pt, Complex Script Font: Times New Roman, 12 pt, Not

Formatted: English (United States)

Formatted: Superscript

Formatted: French (France)

Formatted: Font: (Default) Times New Roman, 12 pt, Font color: Black, Complex Script Font: Times New Roman, 12 pt, French (France), Not Superscript/ Subscript

Formatted: No underline, Font color: Auto, French (France)

Formatted: French (France)

Field Code Changed

Formatted: French (France)

Formatted: French (France)

Formatted: French (France)

Formatted: Centered

33 **1 Introduction**

34 Ocean life relies on the loads of marine macro-nutrients (nitrate, phosphate and orthosilicate) and other  
35 micro-nutrients within the euphotic layer. They fuel phytoplankton growth, maintaining thus the  
36 equilibrium of the food web. These nutrients may reach deeper levels through vertical mixing/~~upwelling~~,  
37 and remineralization of sinking organic matter. Ocean circulation and physical processes continually  
38 drive the large-scale distribution of chemicals (Williams and Follows, 2003) toward a homogeneous  
39 distribution. Therefore, nutrient dynamics is important to understand the overall ecosystem productivity  
40 and carbon cycles. In general, the surface layer is depleted in nutrients in low latitude regions (Sarmiento  
41 and Toggweiler, 1984), but in some ocean regions, called high nutrient low chlorophyll (HNLC) regions,  
42 nutrient concentrations tend to be anomalously high, particularly in areas of the North Atlantic and  
43 Southern Ocean, as well as in the eastern equatorial Pacific, and in the North Pacific; see e.g. Pondaven  
44 et al. (1999). In the Mediterranean, the surface layer is usually nutrient-depleted. Most studies show that  
45 nitrate is the most common limiting factor for primary production in the global ocean (Moore et al.,  
46 2013), while others evidence that phosphate may be a limiting factor in some specific areas, as is the  
47 case of the Mediterranean Sea (Diaz et al., 2001; Krom et al., 2004).

48 Being an enclosed marginal sea, the Mediterranean Sea exhibits an anti-estuarine circulation,  
49 responsible for its oligotrophic character (Bethoux et al., 1992; Krom et al., 2010) and acting like a  
50 subtropical anticyclonic gyre. The Atlantic Water (AW), characterized by low-salinity and low-nutrient  
51 content, enters the Western Mediterranean Sea (WMED) at the surface, through the Strait of Gibraltar,  
52 and moves toward the Eastern Mediterranean Sea (EMED), crossing the Sicily Channel (Fig. 1). In the  
53 Levantine and in the Cretan Sea, the AW becomes saltier, warmer and denser, and it sinks to  
54 intermediate levels (200-500 m) to form the Intermediate Water (IW, Schroeder et al., 2017). The IW  
55 (which may be further called Levantine or Cretan Intermediate Water, LIW or CIW) flows westward  
56 across the entire Mediterranean Sea to the Atlantic Ocean (Fig. 1). As for the deep layer, the Western  
57 Mediterranean Deep Water (WMDW or DW) is formed in the Gulf of Lion through deep convection  
58 (Testor et al., 2018; MEDOC Group, 1970; Durrieu de Madron, et al. 2013) while the Eastern  
59 Mediterranean Deep Water (EMDW) is formed in the Adriatic Sea and occasionally in the Aegean Sea  
60 (Lascazatos et al., 1999; Roether et al., 1996, 2007).

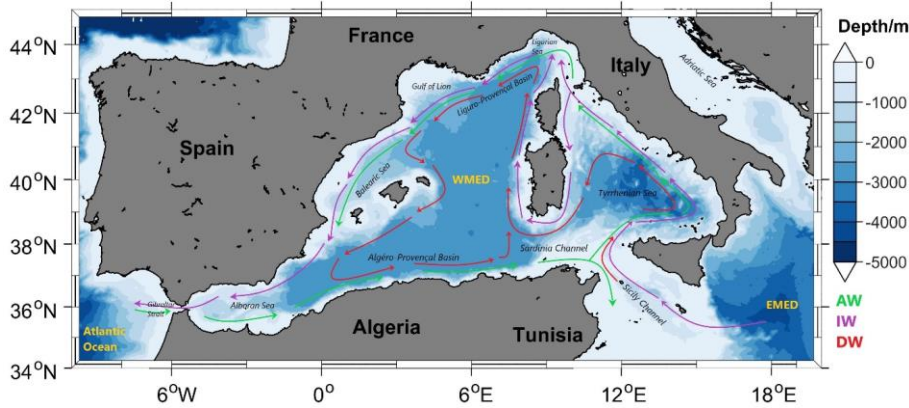
61  
62  
63

**Field Code Changed**

**Formatted:** Do not check spelling or grammar, Not Highlight

**Formatted:** Font: (Default) +Headings CS (Times New Roman), 11 pt, Font color: Auto, Complex Script Font: +Headings CS (Times New Roman), 11 pt, Do not check spelling or grammar

**Formatted:** Do not check spelling or grammar, Not Highlight



64

65 **Figure 1.** Map of the western Mediterranean Sea showing the main regions with a sketch of the AW,  
 66 IW and DW major paths.

67 The Mediterranean Sea is known to be a hotspot for climate change (Giorgi, 2006). During the early  
 68 1990s, the Deep Water (DW) formation area of the EMED shifted from the Adriatic Sea to the Aegean  
 69 Sea. This event is known as the Eastern Mediterranean Transient (EMT; Roether et al., 1996, 2007,  
 70 2014; Roether and Schlitzer, 1991; Theocharis et al., 2002). As a consequence, the intermediate and  
 71 deep waters of the EMED became saltier and warmer (Lascaratos et al., 1999; Malanotte-Rizzoli et al.,  
 72 1999). The EMT affected the WMED as well, not only changing the thermohaline characteristics of the  
 73 IW and concurring to the preconditioning of the Western Mediterranean Transition (WMT; Schroeder  
 74 et al., 2016), which set the beginning of a rapid warming and salting of the deep layers in the WMED  
 75 since 2005 (Schroeder et al., 2006; Schroeder et al., 2010, 2016; Piñeiro et al., 2019). Over the last  
 76 decade, it has been evidenced that heat and salt content have been increasing ~~in~~ all over the deep western  
 77 basin (Schroeder et al., 2016).

78 Changes in circulation due to an increased stratification limit the exchange of materials between the  
 79 nutrient-rich deep layers and the surface layers. Understanding the peculiar oligotrophy of the  
 80 Mediterranean Sea is still a challenge, since there is not an exact quantification of nutrient sinks and  
 81 sources. Studies like Crispi et al. (2001), Ribera d'Alcalà (2003), Krom et al. (2010) and Lazzari et al.  
 82 (2012) related the horizontal spatial patterns in nutrient concentrations mainly to the anti-estuarine  
 83 circulation which exports nutrients to the Atlantic Ocean, showing a decreasing tendency of nutrient  
 84 concentrations toward east, as opposed to the salinity horizontal gradient. Others related it to the  
 85 influence of the atmospheric deposition (Bartoli et al., 2005; Béthoux et al., 2002; Huertas et al., 2012;  
 86 Krom et al., 2010) and rivers discharges that are rich in nitrate and poor deficient in phosphate (Ludwig  
 87 et al., 2009), which might explain the peculiarity in both EMED and WMED.

**Formatted:** Font: (Default) Times New Roman, 11 pt,  
 Complex Script Font: Times New Roman, 11 pt

**Formatted:** Not Highlight

**Formatted:** Font: (Default) Times New Roman, 11 pt,  
 Complex Script Font: Times New Roman, 11 pt

88 Lazzari et al. (2016) also argued that the variations in phosphate are regulated by atmospheric and river  
89 inputs like Ebro and Rhône(Ludwig et al., 2009).

90 These ~~variations, variations,~~ together with the anthropogenic perturbations affect the spatial distribution  
91 of nutrients (Moon et al., 2016) while temporal variability is still unresolved.

92 De Fommervault et al. (2015) reported a decreasing phosphate and an increasing nitrate concentrations  
93 trend between 1990 and 2010, based on a time series (DYFAMED) in the Ligurian Sea, while Moon et  
94 al. (2016) evidenced an increase between 1990 and 2005 and a gradual decline after 2005 in both nitrate  
95 and phosphate in the WMED and EMED.

96 At the global scale, most of the biogeochemical descriptions are based on model simulations and satellite  
97 observations (using sea surface chlorophyll concentrations (Salgado-Hernanz et al., 2019) but also on  
98 the increasing use of Biogeochemical Argo floats (D'Ortenzio et al., 2020; Lavigne, 2015; Testor et al.,  
99 2018), since in situ observations of nutrients are generally infrequent and scattered in space and time.  
100 For this reason, climatological mapping is often applied to sparse in situ data in order to understand the  
101 biogeochemical state of the ocean representing monthly, seasonally, or annually averaged fields.

102 Levitus (1982) was the first to generate objectively analyzed fields of potential temperature, salinity,  
103 and dissolved oxygen, and to produce a climatological atlas of the world ocean.

104 Later on the World Ocean Atlas (WOA), the North Sea climatologies and the Global ocean Carbon  
105 Climatology resulting from GLODAP data product (Key et al., 2004) used the Cressman analysis (1956)  
106 with modified Barnes scheme (Barnes 1964, 1994). In 1994, the first World Ocean Atlas (WOA94;  
107 Conkright et al., 1994) was released integrating temperature, salinity, oxygen, phosphate, nitrate, and  
108 silicate observations. Every four years there is a renewed release of the WOA with an updated World  
109 Ocean database (WOD).

110 On the regional scale, the first salinity and temperature climatology of the Mediterranean Sea was  
111 produced by Hecht et al. (1988) for the Levantine Basin. Picco (1990) was also among the first to  
112 describe the WMED between 1909 and 1987. In 2002, the Medar/Medatlas group (Fichaut et al., 2003)  
113 archived a large amount of biogeochemical and hydrographic in situ observations for the entire region  
114 and used the Variational Inverse Model (VIM; Brasseur, 1991) to build seasonal and interannual gridded  
115 fields. In 2006, the SeadataNet EU project integrated all existing data, to provide temperature and  
116 salinity regional climatology products for the Mediterranean Sea using VIM as well (Simoncelli et al.,  
117 2016), and dissolved inorganic nutrients (nitrate, phosphate and silicate) 6-years centered average from  
118 1965 to 2017 are available on the EMODnet chemistry portal (<https://www.emodnet-chemistry.eu/>).  
119 Within this context, in this study regional climatological fields of in situ nitrate, phosphate and silicate,  
120 using the Data Interpolation Variational Analysis (DIVAnd; Barth et al., 2014) are presented here,  
121 providing a high-resolution field contributing to the existing products (Table 1).

Formatted: Font: (Default) Times New Roman, 11 pt, Complex Script Font: Times New Roman, 11 pt

Formatted: Font: (Default) Times New Roman, 11 pt, Complex Script Font: Times New Roman, 11 pt, Not Highlight

Formatted: Font: (Default) Times New Roman, 11 pt, Complex Script Font: Times New Roman, 11 pt

Formatted: Font: (Default) Times New Roman, 11 pt, Complex Script Font: Times New Roman, 11 pt, Not Highlight

Formatted: Space After: 0 pt

Formatted: Font: (Default) Times New Roman, 11 pt, Complex Script Font: Times New Roman, 11 pt

Formatted: Font: (Default) Times New Roman, 11 pt, Complex Script Font: Times New Roman, 11 pt

Formatted: Font: (Default) Times New Roman, 11 pt, Complex Script Font: Times New Roman, 11 pt

122 The aim of this study is to give a synthetic view of the biogeochemical state of the WMED, to evaluate  
 123 the mean state of inorganic nutrients over 36 years of in situ observations and to investigate upon a  
 124 biogeochemical signature of the effect of the WMT .  
 125 The paper is organized as follows, section 2 describes the data sources used and the quality check;  
 126 section 3 is devoted to the methodology, section 4 presents the main results including a comparison of  
 127 the new climatology with other products. At the end, we address the change in biogeochemical  
 128 characteristics before and after WMT.

129 **Table 1.** Overview of the existing inorganic nutrient climatologies in the Western Mediterranean Sea.

<b>Climatology</b>	WOA	EMODnet	BGC-WMED (Present study)
<b>Reference</b>	(Garcia et al., 2019)	(Míguez et al., 2019)	(Belgacem et al., 2021)
<b>Year of release</b>	2018	2018	2021
<b>Parameter</b>	Nitrate/ Phosphate/ Silicate	Nitrate/ Phosphate/ Silicate	Nitrate/ Phosphate/ Silicate
<b>Unit</b>	$\mu\text{mol kg}^{-1}$	$\mu\text{mol L}^{-1}$	$\mu\text{mol kg}^{-1}$
<b>Data type</b>	<i>CTD Bottle</i>	<i>CTD Bottle</i>	<i>CTD Bottle</i>
<b>Vertical resolution</b>	Seasonal: 43 levels 0-800m Annual: 102 levels 0-5500m	21 standard depth 0-1100m (nitrate) 0-1500m (phosphate) 0-1500m (silicate)	19 levels 0-1500m
<b>Horizontal resolution</b>	1° latitude longitude grid	1/8°	1/4°
<b>Observation time span</b>	1955-2017	1970 to 2016 (nitrate) 1960 to 2016 (phosphate) 1965 to 2016 (silicate)	1981-2017
<b>Area</b>	Global	Mediterranean Sea	Western Mediterranean Sea
<b>Temporal resolution</b>	Season Decadal	Season 6 year running averages	whole observational period, and two sub-intervals (1981-2004, 2005-2017)
<b>Climatology analysis method/ parameter</b>	Objective analysis	DIVA (Data-Interpolating Variational Analysis) tool	DIVAnd (Data-Interpolating Variational Analysis N-dimension)
<b>Correlation length</b>	-	optimized and filtered vertically and a seasonally averaged profile was used.	optimized and filtered vertically and horizontally
<b>Signal to noise ratio</b>	-	A constant value = 1	A constant value = 0.5
<b>Background field</b>	-	the data mean value is subtracted from the data.	the data mean value is subtracted from the data
<b>Detrending</b>	-	No	No
<b>Advection constraint applied</b>	-	No	No

Formatted: Font: Italic, Complex Script Font: Italic

Formatted: Font: (Default) Times New Roman, 10 pt, Italic, Font color: Auto, Complex Script Font: Times New Roman, 10 pt, Bold, Italic, English (United States)

Formatted: Superscript

Formatted: Font: (Default) Times New Roman, 10 pt, Font color: Auto, Complex Script Font: Times New Roman, 10 pt, Bold, English (United States)

Formatted: Font: Italic, Complex Script Font: Italic

Formatted: Superscript

Formatted: Font: Not Italic, Complex Script Font: Not Italic

Formatted: Font: Not Italic, Complex Script Font: Not Italic

Formatted: Font: Not Italic, Complex Script Font: Not Italic

Formatted: Font: Not Italic, Complex Script Font: Not Italic

130

## 131 2 Data

132 The climatological analysis depends on the temporal and spatial distribution of the available in situ data,  
 133 and the reliability of these observations. Due to the scarcity of biogeochemical observations in the  
 134 WMED, merging and compiling data from different sources was necessary.

135 2.1 Data Sources

136 In total, 2253 in situ inorganic nutrient profiles are the base of the biogeochemical climatology of the  
 137 WMED (Table 2) that is described here. These profiles cover the period 1981-2017 and come from ~~four~~  
 138 ~~the major data providers existing in the Mediterranean Sea sources~~, i.e. the Medar/MEDATLAS  
 139 (1981-1996, Fichaut et al., 2003), the recently published CNR\_DIN\_WMED\_20042017  
 140 biogeochemical dataset (2004-2017) (~~Belgacem et al., 2020~~), ~~the SeaDataNet data product (2001-2016)~~  
 141 ~~and other data collected during MedSHIP programs (Schroeder et al., 2015)~~, ~~GLODAPv2~~  
 142 ~~(https://www.glodap.info/) and CARIMED (http://hdl.handle.net/10508/11313) data products~~the  
 143 ~~MOOSE-GE cruises (Mediterranean Ocean Observing System for the Environment- Grande Échelle~~  
 144 ~~programme) (2011-2016, Testor et al., 2011, 2012, 2013, 2014, 2015, 2016) stored in SeaDataNet data~~  
 145 ~~product (2001-2016) and EMODnet (the European Marine Observation and Data Network),~~  
 146 ~~GLODAPv2 (https://www.glodap.info/) and CARIMED (http://hdl.handle.net/10508/11313) data~~  
 147 ~~products and other data collected during MedSHIP programs (Schroeder et al., 2015)~~. All datasets are  
 148 a selection of oceanographic cruises carried out within the framework of European projects ~~such as~~ ~~The~~  
 149 ~~Hydrological cycle in the Mediterranean Experiment (HyMeX) Special Observing Period 2 (Estournel~~  
 150 ~~et al., 2016), the DEnse Water Experiment (DEWEX) project or by regional institutions having as~~  
 151 ~~objectives the investigation of the deep water convection and the biogeochemical properties of the of~~  
 152 ~~the WMED~~. Data were chosen to ensure high spatial coverage (Fig. 3).

153 **Table 2.** Number of inorganic nutrient profiles and data sources.

Source	N. of profiles	N. of observations	Link/ metadata
MEDATLAS	940	8839	<a href="https://odv.awi.de/data/ocean/medatlasii/http://www.ifremer.fr/medar/">https://odv.awi.de/data/ocean/medatlasii/http://www.ifremer.fr/medar/</a>
SEADATANET <u>including MOOSE-GE</u>	523	15388	<a href="http://seadatanet.maris2.nl/v_rsm/content.asp?screen=0&amp;history=yes">http://seadatanet.maris2.nl/v_rsm/content.asp?screen=0&amp;history=yes</a> <a href="https://doi.org/10.17600/11450160">https://doi.org/10.17600/11450160</a> <a href="https://doi.org/10.17600/12020030">https://doi.org/10.17600/12020030</a> <a href="https://doi.org/10.17600/13450110">https://doi.org/10.17600/13450110</a> <a href="https://doi.org/10.17600/14002300">https://doi.org/10.17600/14002300</a> <a href="https://doi.org/10.17600/15002500">https://doi.org/10.17600/15002500</a> <a href="https://doi.org/10.17600/16000700">https://doi.org/10.17600/16000700</a>
CNR_DIN_WMED_20042017	737	8324	<a href="https://doi.org/10.1594/PANGAEA.904172">https://doi.org/10.1594/PANGAEA.904172</a>
Other cruises	53	515	Medship programs; GLODAPv2; CARIMED (not yet available online, personal communication by Marta Álvarez) <a href="https://doi.org/10.1594/PANGAEA.902293">https://doi.org/10.1594/PANGAEA.902293</a>
$\Sigma$	2253	33066	

154

155 2.2 Data distribution

156 The data distribution per year is shown in Figure 2a. Most observations were collected between 1981  
 157 and 1995, and between 2004 and 2017, with a marked gap between 1997 and 2003. Measurement

Formatted: French (France)

Field Code Changed

Formatted: French (France)

Field Code Changed

Field Code Changed

Formatted: Font: (Default) +Headings CS (Times New Roman), Complex Script Font: +Headings CS (Times New Roman), French (France)

Formatted: French (France)

Formatted: Font: (Default) +Headings CS (Times New Roman), 11 pt, Font color: Auto, Complex Script Font: +Headings CS (Times New Roman), 11 pt, French (France), Pattern: Clear

Formatted: French (France)

Formatted: Font: (Default) +Headings CS (Times New Roman), Font color: Auto, Complex Script Font: +Headings CS (Times New Roman), French (France), Pattern: Clear

Formatted: French (France)

Field Code Changed

Formatted: French (France)

Formatted: French (France)

Formatted: French (France)

Formatted: French (France)

Field Code Changed

Field Code Changed

Formatted: Font: (Default) +Headings CS (Times New Roman), 11 pt, Font color: Auto, Complex Script Font: +Headings CS (Times New Roman), 11 pt, Pattern: Clear

Formatted: Font: (Default) +Headings CS (Times New Roman), 11 pt, Font color: Auto, Complex Script Font: +Headings CS (Times New Roman), 11 pt, Pattern: Clear

Formatted Table

Formatted: Font: (Default) Times New Roman, 10 pt, Underline, Font color: Custom Color(5;99;193), Complex Script Font: Times New Roman, 10 pt

Formatted

Formatted: Font color: Auto

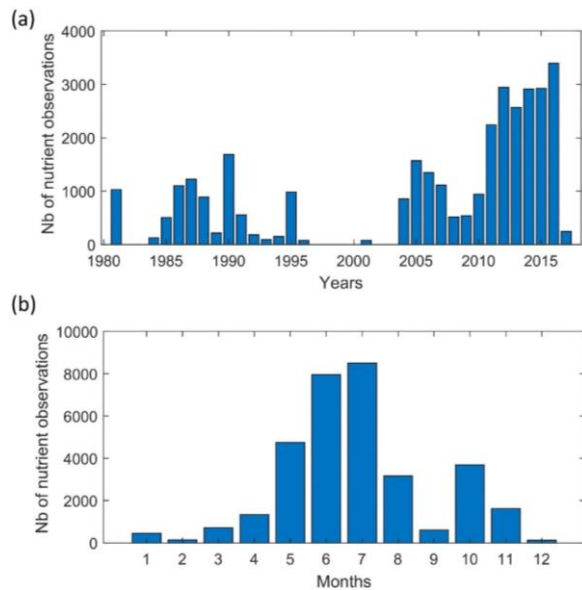
Formatted: Font: Not Italic, Font color: Auto

Formatted: Font: Not Italic, Font color: Auto

Formatted: Line spacing: single

Formatted

158 distribution differs from month to month (Fig.2b) and tends to be biased towards the warm season. Very  
 159 few measurements have been made during December-January-February, while June and July are the  
 160 months with the highest number of available observations (>7000). Consequently, the climatological  
 161 product may be considered as being more representative of spring and summer conditions.



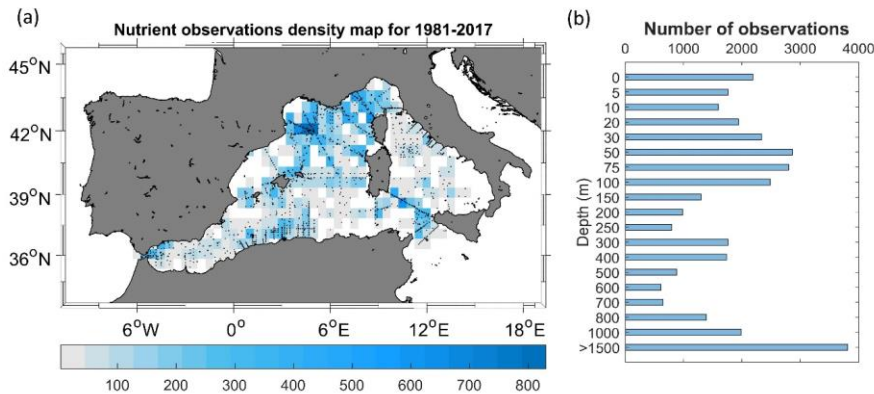
162  
 163 **Figure 2.** Temporal distribution of nutrient observations used for producing the BGC-WMED fields  
 164 (1981-2017), (a) yearly distribution and (b) monthly distribution.

165 Fig. 3a shows the regional distribution of nutrient measurements, while Fig. 3b indicates the number of  
 166 observations found in each depth range around the standard levels chosen for the vertical resolution of  
 167 the climatology.

168 Hydrological and biogeochemical measurements have always been repeatedly collected along several  
 169 repeated transects, known as key regions as the Sicily Channel and the Algéro-Provençal subbasin;  
 170 likewise, the northern WMED is a well sampled area, as it is an area of DW formation. Observation  
 171 density is still scarce (less than 100 observations) in some areas like the northern Tyrrhenian Sea.

172 The total number of measurements at each depth range underlines similar remarks, an uneven  
 173 distribution that needs to be considered in the selection of the vertical resolution to estimate the  
 174 climatological fields. Though, the use of 36 years of nutrient measurements to generate the  
 175 climatological fields significantly reduces the error field. In our case and taking into account the irregular  
 176 distribution in seasons and different years. A climatological gridded field was computed by analyzing

177 observations of three time periods regardless of the month: 1981-2017 and the subsets 1981-2004 and  
178 2005-2017. We chose these subsets to investigate the effect of the WMT on nutrient distribution.



179  
180 **Figure 3.** (a) Nutrient data density used for climatology analysis. Observations are binned in a regular  
181  $1/2^\circ \times 1/2^\circ$  latitude, longitude grid for each year over the period 1981-2017. Location of the stations  
182 included in the analysis are shown as black dots; (b) data distribution per depth range (i.e. at 800 m,  
183 observations between 800-1000 m are included).

### 184 2.3 Data quality check

185 Data were gathered from different data sources, [different analytical methods \(Table A1.\)](#), thus before  
186 merging them, observations were first checked for duplicate (the number of profiles listed in Table 2  
187 refers to all data after removing duplicate measurements). The criteria to detect and remove duplicates  
188 is simple: observations collected during [the same cruises](#) extracted from the different sources were  
189 removed. Since profiles were measured during specific cruise (identified with a unique identification  
190 code) at specific time, ~~data from duplicate cruises~~ are removed.

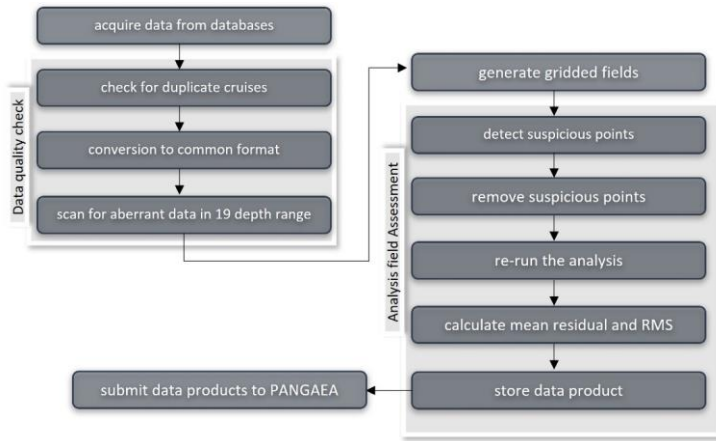
191 Then, data ~~were~~ converted to a common format (similar to the csv CNR\_DIN\_WMED\_20042017  
192 data product, Belgacem et al., 2019). This recently released product contains measurements covering  
193 the WMED from 2004 to 2017. The data of the CNR\_DIN\_WMED\_20042017 product have undergone  
194 a rigorous quality control process that was focused on a primary quality check of the precision of the  
195 data and a secondary quality control targeting the accuracy of the data, [details about the adjustments and](#)  
196 [the applied corrections are found in Belgacem et al.\(2020\).](#) ~~Adjustments were applied to measurements~~  
197 ~~when bias was detected.~~

198 As detailed in Table 2, we combined observations from reliable sources (covering the time period 1981-  
199 2017), ~~that~~ were quality controlled according to international recommendations before being published  
200 (Maillard et al., 2007; SeaDataNet Group, 2010). Though, these historical data collections coming from



201 sources different from the CNR\_DIN\_WMED\_20042017 have been subjected to a quality check before  
 202 merging them, to eliminate the effect of any aberrant observation. The check was carried out by  
 203 computing median absolute deviations in 19 pressure classes (referring to the selected vertical resolution  
 204 of section 2.1)(0-10, 10-30, 30-60, 60-80, 80-160, 160-260, 260-360, 360-460, 460-560, 560-900, 900-  
 205 1200, 1200-1400, 1400-1600, 1600-1800, 1800-2000, 2000-2200, 2200-2400, 2400-2600, >2600 dbar).  
 206 Any value that is more than three median absolute deviations from the median value is considered a  
 207 suspected measurement.

208 In total, 2.35% of nitrate observations, 2.44% of phosphate observations and 2.14% of silicate  
 209 observations were removed.



210  
 211 **Figure 4.** Flowchart describing the steps during the quality control: see text in section 2.3 and 3.3 for  
 212 [more details.](#)

### 213 3 Methods

#### 214 3.1 Variational analysis mapping tool

215 Here, the **Data-Interpolating Variational Analysis- n dimension (DIVAnd)** method (Beckers et al., 2014;  
 216 Troupin et al., 2010, 2012) was used to generate the gridded fields. DIVA has been widely applied to  
 217 oceanographic climatologies, such as the SeaDataNet climatological products (Simoncelli et al., 2014,  
 218 2016, 2019, 2020a, 2020b, 2020c, 2021; Iona et al., 2018), EMODnet chemistry regional climatologies  
 219 (Míguez et al., 2019), the Adriatic Sea climatologies by Lipizer et al. (2014) or the black Sea (Capet et  
 220 al., 2014) and it was also applied to generate the global interior climatology GLODAPv2. 2016b

**Formatted:** Font: Bold, Complex Script Font: Bold  
**Formatted:** Not Highlight  
**Formatted:** Caption, Left, Line spacing: single  
**Formatted:** Font: Not Bold, Complex Script Font: Not Bold  
**Formatted:** Font: 11 pt, Bold, Font color: Auto, Complex Script Font: 11 pt, Highlight

221 (Lauvset et al., 2016). It is an efficient mapping tool used to build a continuous spatial field from  
 222 discrete, scattered, irregular in situ data points with an error estimate at each level.

223 The BGC-WMED gridded fields have been computed with the more advanced N-dimensional version  
 224 of DIVA, DIVAnd v2.5.1 (Barth et al., 2014) (<https://doi.org/10.5281/zenodo.3627113>) using Julia as  
 225 a programming language (<https://julialang.org/>) under the Jupyter environment (<https://jupyter.org/>).  
 226 The code is freely available at <https://github.com/gher-ulg/DIVAnd.jl> (last access: January, 2020).

227 DIVA is based on the variational inverse method (VIM) (Brasseur et al., 1996). It takes into account the  
 228 errors associated with the measurements and takes account of the topography/bathymetry of the study  
 229 area. The method is designed to estimate an approximated field  $\varphi$  close to the observations and find the  
 230 field that minimizes the cost function  $J[\varphi]$ .

231 The cost function is defined as the misfit between the original data  $d_i$ , an array of  $N_d$  observations, the  
 232 analysis (observation constraint term) and a smoothness term. (Troupin et al., 2010):

233 
$$J[\varphi] = \sum_{i=1}^{N_d} \mu_i Lc^2 (d_i - \varphi(x_i, y_i))^2 \quad (1) \text{ Observation constraint term}$$

234 
$$+ \int_D (\alpha_2 \nabla \nabla \varphi : \nabla \nabla \varphi + \alpha_1 Lc^2 \nabla \varphi \cdot \nabla \varphi + \alpha_0 Lc^4 \varphi^2) dD \quad (2) \text{ Smoothness term}$$

235

236 Eq. (1)

237 where  $Lc$  is the correlation length,  $\nabla$  is the gradient operator,  $\nabla \nabla \varphi : \nabla \nabla \varphi$  is the squared Laplacian of  $\varphi$ ,  
 238 the first term (observation constraint) considers the distance between the observations and the analysis  
 239 reconstructed field  $\varphi(x_i, y_i)$ , so that  $\mu_i$  penalizes the analysis misfits relative to the observations. if the  
 240 observation constraint is only composed of  $d_i - \varphi(x_i, y_i)$ , the constructed field would be a simple  
 241 interpolation of the observations and the minimum is reached when  $d_i = \varphi(x_i, y_i)$ . The field  $\varphi(x_i, y_i)$   
 242 need to be close to the observation and not have large variation. The second term (smoothness term)  
 243 measures the regularity of the domain of interest  $D$ . This expression within the integral remains  
 244 invariant (Brasseur and Haus, 1991).  $\alpha_0$  minimize the anomalies of the field itself,  $\alpha_1$  minimize the  
 245 spatial gradients,  $\alpha_2$  penalizes the field variability (regularization). The reconstructed fields are  
 246 determined at the elements of a grid on each isobath using the cost function Eq. (1).

247 The grid is dependent on the correlation length and the topographic contours of the specified grid in the  
 248 considered region, so there is no need to divide the region before interpolating.

Formatted: Not Highlight
Formatted: Not Highlight
Formatted: Not Highlight
Formatted: Not Highlight
Formatted: Not Highlight
Formatted: Not Highlight
Formatted: Not Highlight
Formatted: Font: 11 pt, Complex Script Font: 11 pt
Formatted: Font: 11 pt, Complex Script Font: 11 pt
Formatted: Font: 11 pt, Complex Script Font: 11 pt
Formatted: Font: 11 pt, Complex Script Font: 11 pt, Not Highlight
Formatted: Font: 11 pt, Complex Script Font: 11 pt, Not Highlight
Formatted: Font: 11 pt, Complex Script Font: 11 pt, Not Highlight
Formatted: Font: 11 pt, Complex Script Font: 11 pt, Not Highlight
Formatted: Font: 11 pt, Complex Script Font: 11 pt, Not Highlight
Formatted: Font: 11 pt, Complex Script Font: 11 pt, Not Highlight
Formatted: Font: 11 pt, Complex Script Font: 11 pt, Not Highlight
Formatted: Font: 11 pt, Complex Script Font: 11 pt, Not Highlight
Formatted: Font: 11 pt, Complex Script Font: 11 pt, Not Highlight
Formatted: Font: 11 pt, Complex Script Font: 11 pt, Not Highlight
Formatted: Font: 11 pt, Complex Script Font: 11 pt, Not Highlight
Formatted: Font: 11 pt, Complex Script Font: 11 pt, Not Highlight
Formatted: Font: 11 pt, Complex Script Font: 11 pt, Not Highlight
Formatted: Font: 11 pt, Complex Script Font: 11 pt, Not Highlight
Formatted: Font: 11 pt, Complex Script Font: 11 pt, Not Highlight
Formatted: Font: 11 pt, Complex Script Font: 11 pt, Not Highlight
Formatted: Font: 11 pt, Complex Script Font: 11 pt, Not Highlight
Formatted: Font: 11 pt, Complex Script Font: 11 pt, Not Highlight
Formatted: Font: 11 pt, Complex Script Font: 11 pt, Not Highlight
Formatted: Font: 11 pt, Complex Script Font: 11 pt, Not Highlight
Formatted: Font: 11 pt, Complex Script Font: 11 pt, Not Highlight
Formatted: Font: 11 pt, Complex Script Font: 11 pt, Not Highlight
Formatted: Font: 11 pt, Complex Script Font: 11 pt, Not Highlight
Formatted: Font: 11 pt, Complex Script Font: 11 pt, Not Highlight
Formatted: Font: 11 pt, Complex Script Font: 11 pt, Not Highlight
Formatted: Font: 11 pt, Complex Script Font: 11 pt, Not Highlight
Formatted: Font: 11 pt, Complex Script Font: 11 pt, Not Highlight
Formatted: Font: 11 pt, Complex Script Font: 11 pt, Not Highlight
Formatted: Font: 11 pt, Complex Script Font: 11 pt, Not Highlight
Formatted: Font: 11 pt, Complex Script Font: 11 pt, Not Highlight
Formatted: Font: 11 pt, Complex Script Font: 11 pt, Not Highlight
Formatted: Font: 11 pt, Complex Script Font: 11 pt, Not Highlight
Formatted: Font: 11 pt, Complex Script Font: 11 pt, Not Highlight
Formatted: Font: 11 pt, Complex Script Font: 11 pt, Not Highlight
Formatted: Font: 11 pt, Complex Script Font: 11 pt, Not Highlight
Formatted: Font: 11 pt, Complex Script Font: 11 pt, Not Highlight
Formatted: Font: 11 pt, Complex Script Font: 11 pt, Not Highlight
Formatted: Font: 11 pt, Complex Script Font: 11 pt, Not Highlight
Formatted: Font: 11 pt, Complex Script Font: 11 pt, Not Highlight
Formatted: Font: 11 pt, Complex Script Font: 11 pt, Not Highlight
Formatted: Font: 12 pt, Complex Script Font: 12 pt

249 The method computes two-, three- to four-multi-dimensional analyses (longitude, latitude, depth, time).  
250 For climatological studies, the four-dimensional extension was used on successive horizontal layers at  
251 different depths for the whole time period.

252 Along with the gridded fields, DIVA yields error fields dependent on the data coverage and the noise in  
253 the measurements (Brankart and Brasseur, 1998; Rixen et al., 2000). Full details about the approach ~~is~~  
254 are provided extensively by Barth et al. (2014) and Troupin et al. (2018) in the Diva User Guide  
255 (<https://doi.org/10.5281/zenodo.836723>).

### 256 3.2 Interpolation parameters

257 DIVA is conditioned by topography, by the spatial correlation length ( $L_c$ ) and by the signal-to-noise  
258 ratio (SNR,  $\lambda$ ) of the measurements, which are essential parameters to obtain meaningful results. They  
259 are considered more in detail in the following sections.

#### 260 3.2.1 Land-sea mask

261 A 3D dimension land-sea mask is created using the coastline and bathymetry of the General Bathymetric  
262 Chart of the Oceans (GEBCO) 30-sec topography (Weatherall et al., 2015). The WMED is a relatively  
263 small area which necessitates a high-resolution bathymetry to generate a mask at different depth layers.  
264 The vertical resolution is set to 19 standard depth levels from the surface to 1500 m: 0, 5, 10, 20, 30, 50,  
265 75, 100, 150, 200, 250, 300, 400, 500, 600, 700, 800, 1000, 1500 m, corresponding to the most  
266 commonly used predefined levels for the sampling of seawater for nutrient analyses. The resulting fields  
267 at each depth level are the interpolation on the specified grid. These depth surfaces are the domain on  
268 which the interpolation is performed.

#### 269 3.2.2 The spatial correlation length scale ( $L_c$ )

270  $L_c$  indicates the distance over which an observation affects its neighbors. The correlation length can be  
271 set by the user or computed using the data distribution.

272 For the BGC-WMED biogeochemical climatology, this parameter was optimized for the whole-time  
273 span, and at each depth layer. The correlation length has been evaluated by fitting the empirical kernel  
274 function to the correlation between data isotropy and homogeneity in correlations. The quality of the fit  
275 is dependent on the number of observations (Troupin et al., 2018). The analytical covariance model used  
276 in the fit is derived for an infinite domain (Barth et al, 2014). To assess the quality of the fit, the data  
277 covariance and the fitted covariance are plotted against the distance between data points (Fig. 45). At  
278 10 m, the correlation length was obtained with a high number of data points, indicating that the empirical  
279 covariance used to estimate the covariance and the fitted covariance are in good agreement.

**Formatted:** No widow/orphan control, Don't adjust space between Latin and Asian text, Don't adjust space between Asian text and numbers, Border: Top: (No border), Bottom: (No border), Left: (No border), Right: (No border), Between : (No border)

**Formatted:** Not Highlight

**Formatted:** Default Paragraph Font, Font: (Default) Calibri, Font color: Auto, Complex Script Font: Calibri, Pattern: Clear

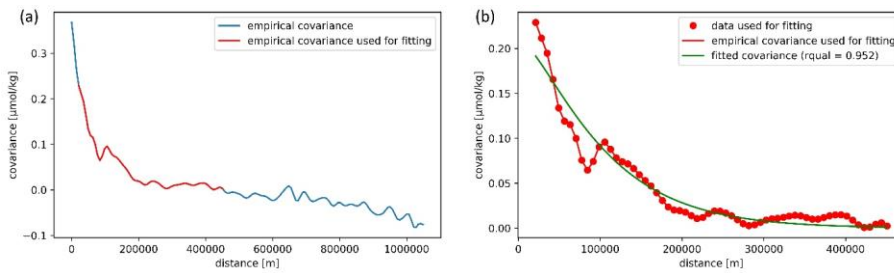
**Formatted:** Font color: Auto, Complex Script Font: 11 pt, Check spelling and grammar

**Formatted:** Not Highlight

280 At some depth layers there are irregularities due to an insufficient amount of data points, making it  
 281 necessary to apply a smoothing filter/fit to minimize the effect of these irregularities. It has been tested  
 282 whether a randomly selected field analysis (nitrate data from 2006 and 2015) obtained with the fitted-  
 283 vertical correlation profile is better than the analysis with zero-vertical correlation. A skill score relative  
 284 to analysis non-fitted-vertical correlation has been computed following Murphy (1988) and Barth et  
 285 al.(2014):

$$286 \text{ skill score} = 1 - \frac{RMS_{no\ fit}^2}{RMS^2} \quad \text{Eq. (2)}$$

287 A large difference in the global RMS between the analysis with the fitted-vertical correlation and the  
 288 analysis with non-fitted-vertical correlation used for validation was found. The test shows whether the  
 289 use of the fit in the correlation profile is improving the overall analysis or not. We found that the RMS  
 290 error (nitrate analysis of 1981-2017) was reduced from  $0.696 \mu\text{mol kg}^{-1}$  (analysis without fit) to  $0.571$   
 291  $\mu\text{mol kg}^{-1}$  (analysis with fit) at 10 m depth, which means using the fitted vertical correlation profile in  
 292 the analysis improves the skill by 32 %, and the fit is improving the analysis fields.



293  
 294 **Figure 54.** Example of the Nitrate covariance. (a) The empirical data covariance function is given in  
 295 red, the curve comes from the analysis of observations within depth = 10 m, while (b) the fitted  
 296 covariance curve (theoretical kernel) is given in green.

297 Based on the data, DIVA performs a least-square fit of the data covariance function with a theoretical  
 298 function. Then, a vertical filter is applied and an average profile over the whole period is used (Fig. 56).  
 299 This procedure is analogous to what has been used for the EMODnet climatology and the North Atlantic  
 300 climatology, except that in EMODnet climatology, seasonally averaged profiles were used (Buga et al.,  
 301 2019) and a monthly averaged profiles were used in North Atlantic climatology (Troupin et al., 2010).  
 302 The filter is applied to discard aberration caused by outliers or scarce observations in some layers, as  
 303 described above.

304 Because of the horizontal and vertical inhomogeneity of the data coverage, the analysis was based on a  
 305 correlation length that varies both horizontally (Fig. 5a6a) and vertically (Fig. 5b6b).

306 As expected, Lc increases with depth (Fig. 56), extending the influence area of the observation, a  
307 consequence of the fact that variability at depth is lower and that observations in the deep layer are  
308 scarcer (which on the other hand makes the Lc estimate more uncertain).

309 From the surface to 150-200 m, Lc is rather constant (Fig. 6), while from 200 to 600 m, the horizontal  
310 Lc (Fig. 6a) increases for all nutrients. Below 600 m, the horizontal Lc for silicate decreases down to  
311 1000 m, and then increases again at 1500 m. For nitrate and phosphate, a similar, but less marked,  
312 behavior is observed.

313

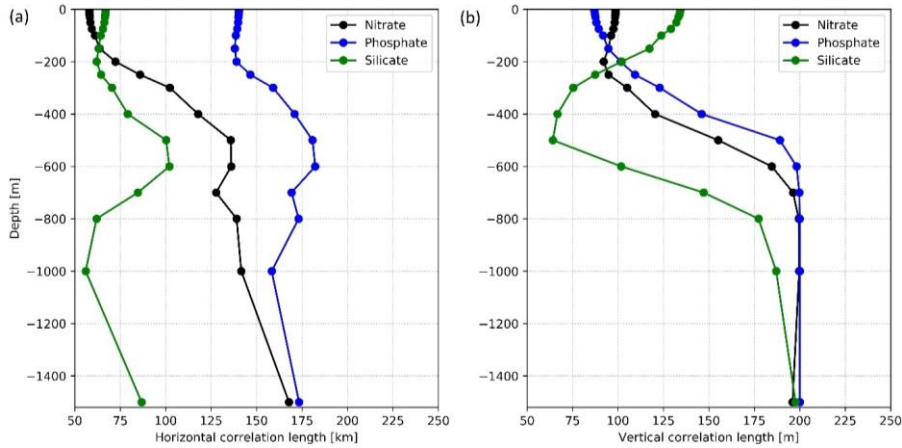
314 The vertical Lc (Fig. 6b) behaves similarly toward the increase, for nitrate and phosphate, due to the  
315 homogeneity of the intermediate water mass, as explained also by Troupin et al. (2010). For silicate, the  
316 vertical Lc decreases in the intermediate depth, reaching a minimum at 500 m depth. The different  
317 behavior of silicate could be explained by the progressive increase in concentrations from the surface to  
318 the deep layer, compared to nitrate and phosphate vertical distribution (strong gradient between surface  
319 depleted layer and intermediate layer). Lc for silicate has lower values compared to nitrate and  
320 phosphate, because, horizontally and vertically, it behaves in a different way. Unlike nitrate and  
321 phosphate, silicate does not show a strong east-west increased gradient. This gradient might induce this  
322 difference in the horizontal distance over which the sample influences its neighborhood.

323 Besides, Silicate is less utilized by primary producers, and the dissolution of the biogenic silica is  
324 slower than that of the other nutrients (DeMaster, 2002) which explain its progressive increase towards  
325 deeper layers (Krom et al., 2014).

326 ~~Below 600 m, the horizontal Lc for silicate decreases down to 1000 m, and then increases again at 1500~~  
327 ~~m. For nitrate and phosphate, a similar, but less marked, behavior is observed.~~ The vertical Lc for all  
328 nutrients increases progressively from 400 m to 1500 m.

329 Troupin et al. (2010) and Iona et al. (2018) attributed similar changes observed in Lc for temperature  
330 and salinity to the variability of the water masses in each layer. This might also explain the changes  
331 found in Lc for nutrients. Indeed, the concentration of nutrients in the WMED increases with depth and  
332 is very low at the surface, which explains the constant low values of Lc in this layer.

**Formatted:** Font: (Default) Times New Roman, 11 pt,  
Font color: Auto, Complex Script Font: Times New  
Roman, 11 pt



333  
 334 **Figure 65.** (a) Horizontal and (b) vertical optimized correlation lengths, for each nutrient (1981-2017),  
 335 as a function of depth.

### 336 3.2.3 Signal-to-Noise Ratio

337 The signal-to-noise ratio (SNR) is related to the confidence in the measurements. It is the ratio between  
 338 the variance of the signal and the variance of the measurement noise/error. The SNR defines the  
 339 representativeness of the measurements relative to the climatological fields, in other words it is the  
 340 confidence in the data.

341 It not only depends on the instrumental error but also on the fact that observations are instantaneous  
 342 measurements, and since a climatology is a long-term mean, such observations do not represent exactly  
 343 the same.

344 Generally, small SNR values favor large deviations from the real measurements to give a smoother  
 345 climatological field. On the other hand, with a high SNR, DIVAnd keeps the existing observations and  
 346 interpolates between data points. The need is to find an approximation that does not deviate much from  
 347 the real observations (further details in Lauvset et al., 2016, and Troupin et al., 2010).

348 Following the same approach that many climatologies that used the DIVAnd method adopted, i.e.  
 349 EMODnet climatologies (available on the EMODnet chemistry portal), the Atlantic regional  
 350 climatologies (Troupin et al., 2010), the Adriatic Sea climatology (Lipizer et al., 2014) and the  
 351 SeadataNet regional climatology (Simoncelli et al., 2015), the SNR is set to a constant value (Table 1).

352 The analysis is performed with a predefined uniform default error variance of 0.5 for all parameters at  
 353 all depths, we presume that the data sources used to generate BGC-WMED climatology are consistent  
 354 products. Three iterations are done inside DIVAnd to estimate the optimal scale factor of error variance

355 of the observation (following Desroziers et al., 2005). More details can be found in [https://gher-  
ulg.github.io/DIVAnd.jl/latest/#DIVAnd.diva3d](https://gher-<br/>356 ulg.github.io/DIVAnd.jl/latest/#DIVAnd.diva3d).

357 Values of SNR provided by means of a generalized cross-validation (GCV) technique (Brankart and  
358 Brasseur, 1998) gave a large estimate of the SNR (of the order of 22) showing a discontinuous analysis  
359 field and patterns around the cruise transects and do not represent properly the climatological fields.

~~360 High SNR means less confidence in the observation, while we presume that the data sources used to  
361 generate BGC-WMED climatology are consistent products.~~

### 362 3.3 Detection of suspicious data

363 Assessment of the analysis is performed by detecting outliers and suspicious data , in order to remove  
364 observations that generate irregular interpolated fields and suspect observations that were not detected  
365 in the data quality check of section 2.3.

366 The automatic check measures how consistent the gridded field is with respect to the nearby  
367 observations by estimating the difference between a measurement and its analysis scaled by the expected  
368 error and, based on that, a score is assigned to each observations. Data points with the highest scores  
369 were considered as suspect and were removed from the analysis (Fig. A1, 2, 3). Overall, 0.031%,  
370 0.014%, 0.004% data points, for nitrate, phosphate, and silicate, respectively, were considered  
371 inconsistent. ~~Details about t~~The quality check values and range that were used are available plotted in  
372 the netCDF files of the product appendix (Table A1).

### 373 3.4 Quality check of the analysis fields

374 The quality of the climatology was checked against observations by estimating the mean residual and  
375 the root mean squared (RMS) of the difference between the climatology and the observations. Averages  
376 over the entire basin were calculated between depth ~~levels~~ surfaces (see section 2.3).

377 Residuals are the difference between the observations within the specific depth surface and the analysis  
378 (interpolated linearly to the location of the observations) and are estimated by depth range (Fig. 7).  
379 ~~The residuals are NaN when the observations fall outside the selected domain for the climatology, as~~  
380 ~~defined by the mask and the coordinates of the observations.~~The analysis fields at each depth range (i.e.  
381 depth surfaces or domain on which the interpolation is performed) are the interpolation on the specified  
382 grid. In Fig. 7, we present the vertical profile of the mean residuals and RMS at different depth ranges  
383 for the three nutrients.

384 ~~The result of~~

385 ~~Fig. 6a shows nitrate residuals~~Nitrate observations and the analysis field in Fig.7a have a high level of  
386 agreement i-n the surface layer (-from the 0 to 30 m depth), the observations and the analysis have a

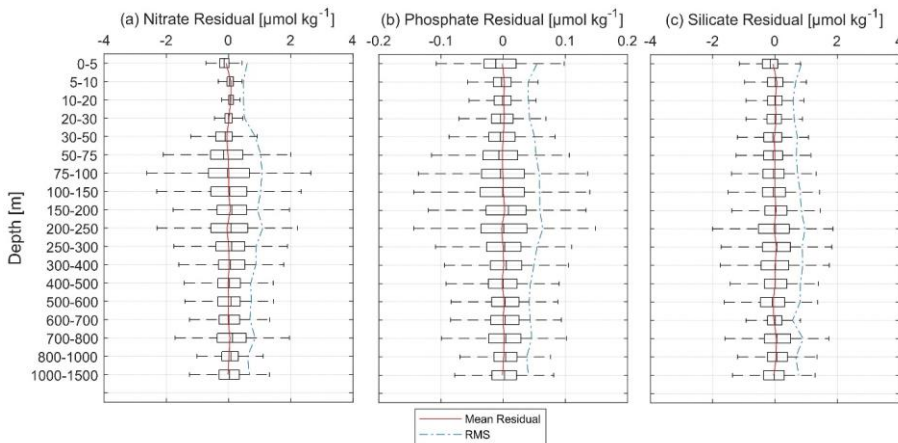
387 ~~high level of agreement. Just below (between 30 and 200 m),~~ boxplots are suggestive of larger  
 388 differences. From surface to the deep layer, the mean residual between nitrate observation and the  
 389 gridded field varied between -0.075 and 0.0765  $\mu\text{mol kg}^{-1}$ , while ~~the~~ the corresponding RMS for nitrate  
 390 fluctuated varied between 0.47 and 1.1  $\mu\text{mol kg}^{-1}$ . ~~This is justified by the inhomogeneity of the~~  
 391 observations mainly in deep layers.

392 ~~As for phosphate residuals (Fig. 6b), low level of agreement was found between 75 and 200 m and a~~  
 393 ~~lower difference in the surface and below 250 m.~~ As for the average residual between phosphate  
 394 observations and the gridded analysis (Fig. 7b) was around zero and varied between -0.0027 and 0.0026  
 395  $\mu\text{mol kg}^{-1}$ . The RMS for phosphate ~~varied was~~ between 0.037 and 0.063  $\mu\text{mol kg}^{-1}$ .

396 Silicate residuals (Fig. ~~6e~~7c), on the other hand, seemed more homogeneous at all depth levels. The  
 397 highest level of agreement was found below 20 m and at 600 m. Overall residuals varied between -0.057  
 398 and 0.063  $\mu\text{mol kg}^{-1}$ , while the RMS ranged between 0.567 and 0.963  $\mu\text{mol kg}^{-1}$ .

399 Over the entire water column, the mean residual was around zero (0.004  $\mu\text{mol kg}^{-1}$  for nitrate, 0.0002  
 400  $\mu\text{mol kg}^{-1}$  for phosphate and 0.003  $\mu\text{mol kg}^{-1}$  for silicate) (Fig. 67); The RMS blue line fell within the  
 401 mean residual +/- standard deviation in the upper 25<sup>th</sup> percentile at the different depth ranges and in all  
 402 parameters; meaning that in general, the bias between the observations and the analysis is small and  
 403 there is a good agreement.

Formatted: Superscript



404  
 405 **Figure 76.** Vertical mean residuals (in red), i.e. the differences between the observations and the analysis  
 406 and the mean RMS (dashed blue) of (a) nitrate, (b) phosphate, (c) silicate.



407 **4 Results**

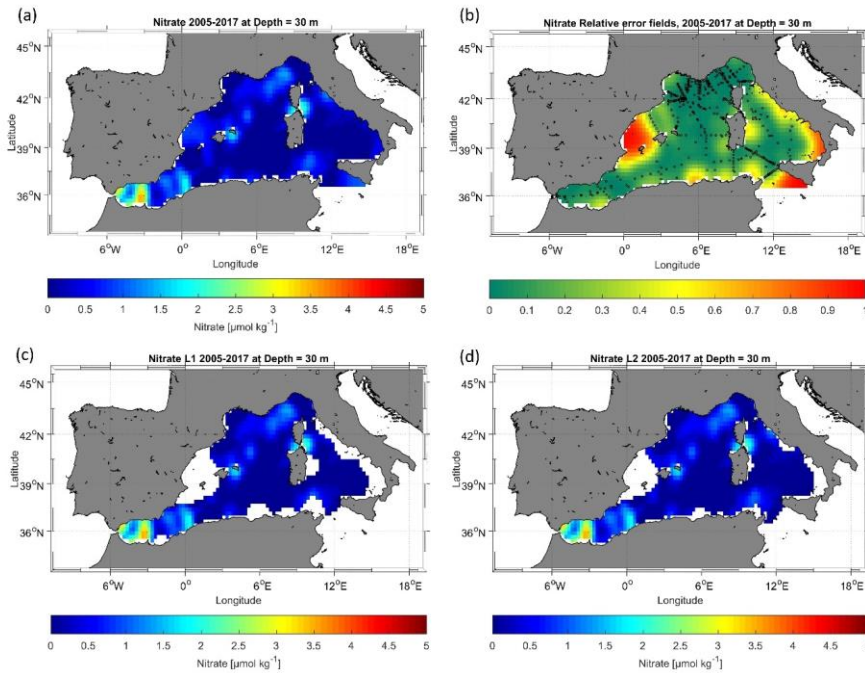
408 The final result consists of gridded fields of mapped climatological means of inorganic nutrients for the  
 409 periods 1981-2004, 2005-2017, and the whole period 1981-2017, produced with VIM described in  
 410 section 3, using data of section 2. Together with the gridded fields, error maps have been generated to  
 411 check the degree of reliability of the analysis.

412 The resulting climatologies (Table 3) are aggregated in a 4D netCDF for each nutrient and each time  
 413 period that contains the interpolated field of the variable and related information: associated relative  
 414 error, variable fields masked using two relative error thresholds (L1 and L2). The mapped climatology  
 415 is available from PANGAEA (<https://doi.pangaea.de/10.1594/PANGAEA.930447>, Belgacem et al.,  
 416 2021) as one folder named BGC-WMED climatology. This folder contains nine [files: three per  
 417 parameter and three per time period netCDF files for each parameter and time period.](#)

418 Here is an example of the analysis output found in the netCDF. Figure 7-8 shows the unmasked  
 419 climatological field of the mean spatial variation of nitrate, relative error field distribution, the masked  
 420 climatological field using relative error with two threshold values (0.3 and 0.5) to assess the quality of  
 421 the resulting fields.

423 **Table 3.** Available analyzed fields and available information in the netCDF files.

Variable name	Field name	Description
Lon	Longitude	Longitude in degrees east, extent: -7 – 17.25 °E
Lat	Latitude	Latitude in degrees north, extent: 33.5 – 45.85°N
depth	Depth	Depth in meters, 19 levels, range: 0 – 1500 m
nitrate/phosphate/silicate	DIVAnd analyzed climatology	Mapped climatological fields
nitrate_L1/phosphate_L1/ silicate_L1	Nitrate/Phosphate/Silicate masked field level 1	Mapped climatological fields masked using relative error threshold 0.3.
nitrate_L2/ phosphate_L2/ silicate_L2	Nitrate/Phosphate/Silicate masked field level 2	Mapped climatological fields masked using relative error threshold 0.5.
nitrate_relerr/phosphate_re lerr/silicate_relerr	Nitrate/Phosphate/Silicate masked relative error	Mapped relative error filed associated to the climatological field



425

426 **Figure 87.** Example of nitrate analysis for the period 2005-2017 (a) unmasked analysis field, (b) relative  
 427 error field distribution with the observation in black circles, (c) masked analysis fields masked using  
 428 relative error threshold = 0.3, and (d) masked analysis fields masked using relative error threshold = 0.5.

#### 429 4.1 Nutrient climatological distribution

430 A description of the spatial patterns of the dissolved inorganic nutrients across the domain and over the  
 431 entire period (1981-2017) is given. The gridded fields for nitrate, phosphate, and silicate are discussed  
 432 at three depth levels, representative of the surface (at 100 m), intermediate (at 300 m), and deep layer  
 433 (at 1500 m). The horizontal maps at the selected depths are shown in Fig. 89, while the average vertical  
 434 profiles of nutrients over the whole area are shown in Fig. 910.

##### 435 4.1.1 Surface layer

436 The nitrate, phosphate and silicate mean climatological fields over 1981-2017 are presented in Fig. 89  
 437 (a, b, c) respectively. The mean surface nitrate at 100 m is about  $3.58 \pm 1.16 \mu\text{mol kg}^{-1}$ . Highest surface  
 438 values of nitrate concentrations are found in regions where strong upwelling or vertical mixing occurs,  
 439 such as the Liguro-Provençal basin and the Alboran Sea (see Fig. 8a9a), and regions with extensive  
 440 supply by the Ebro, Rhone, Moulouya and Shellif rivers-

441 The convection region (Gulf of Lion and Ligurian Sea) is characterized by an eutrophic regime and a  
442 spring bloom (Lavigne et al., 2015), unlike the rest of the basin that shows low nitrate concentrations in  
443 the surface layer ( $< 4 \mu\text{mol kg}^{-1}$ ).

444 Nutrient patterns in the Alboran Sea have been associated with the distinct vertical mixing that supplies  
445 the surface layer with nutrients (Lazzari et al., 2012; Reale et al., 2020).

446 Indeed, the northern Alboran Sea is known as an upwelling area, where permanent strong winds enhance  
447 the regional biological productivity (Reul et al., 2005). Nitrate distribution at 100 m presents a clear  
448 distinction between the enriched surface regions in the WMED, under the influence of deep convection  
449 processes, and the easternmost depleted region.

450 The distribution of phosphate concentration has striking similarities with that of nitrate (Fig. 8b9b). The  
451 mean surface phosphate concentrations at 100 m, is  $0.16 \pm 0.06 \mu\text{mol kg}^{-1}$ . As for nitrate, the highest  
452 surface values are found in the Alboran Sea, Balearic Sea, Gulf of Lion and Liguro-Provençal Basin  
453 ( $0.2\text{-}0.3 \mu\text{mol kg}^{-1}$ ), while the Tyrrhenian Sea and the Algerian Sea revealed phosphate concentration  
454 that were  $< 0.2 \mu\text{mol kg}^{-1}$ . Similar patterns were observed by Lazzari et al. (2016), who argued that the  
455 variations in phosphate are regulated by atmospheric and terrestrial inputs. It should be noted that the  
456 maximum in the surface is found near river discharges of freshwater, like Ebro and Rhône, i.e. the largest  
457 rivers of the WMED (Ludwig et al., 2009).

458 Concerning the distribution of silicate concentration, the surface layer at 100 m (Fig. 8e9c) followed the  
459 same pattern as nitrate and phosphate. Over this layer the mean silicate was about  $2.7 \pm 0.7 \mu\text{mol kg}^{-1}$ .  
460 As for nitrate and phosphate, the highest values ( $3\text{-}4 \mu\text{mol kg}^{-1}$ ), were recorded in the Alboran Sea,  
461 Balearic Sea, Gulf of Lion and Liguro-Provençal Basin and in the southern entrance of the Tyrrhenian  
462 Sea. This surface distribution is in good agreement with the findings of Crombet et al. (2011), relating  
463 this local silicate surface maximum to the continental input, river discharge and atmospheric deposition  
464 (Frings et al., 2016; Sospedra et al., 2018). The spatial minima were reported in the Tyrrhenian Sea and  
465 Algerian Sea ( $< 3 \mu\text{mol kg}^{-1}$ ).

#### 466 4.1.2 Deep and Intermediate layer

467 At the basin scale, nitrate concentrations increase with depth (Fig. 9a10a), with the highest concentration  
468 found at intermediate levels (250-500 m), ranging between  $8.8$  and  $9.0 \mu\text{mol kg}^{-1}$ . In this 300 m (Fig.  
469 8d9d), nitrate concentrations average is  $7.2 \pm 1.06 \mu\text{mol kg}^{-1}$ . High values ( $> 6.5 \mu\text{mol kg}^{-1}$ ) are found  
470 in the westernmost regions (Alboran Sea, Algerian Sea, Gulf of Lion, Balearic Sea and the Liguro-  
471 Provençal Basin), while the easternmost regions (Tyrrhenian Sea, Sicily Channel), exhibit much lower  
472 concentrations (between  $4.5$  and  $6.5 \mu\text{mol kg}^{-1}$ ).

473 Similar features are observed in the deep layer, at 1500 m (Fig. 8a9a), with nitrate concentrations  
474 increasing all over the basin, reaching on average  $7.8 - 7.9 \mu\text{mol kg}^{-1}$  between 1000 and 1500 m depth  
475 (Fig. 9a10a).

476 In both layers (300 m and 1500 m), the difference between the eastern opening of the basin (Sicily  
477 Channel) and the western side (Alboran Sea) is noticeable: the Sicily Channel and the Tyrrhenian Sea  
478 are under the direct influence of the water masses coming from the oligotrophic EMED, which then  
479 gradually become enriched with nutrients along its path, as found by Schroeder et al. (2020).

480 Phosphate concentrations at intermediate depth (see 300 m, Fig. 8e9e), varied between 0.12 and 0.44  
481  $\mu\text{mol kg}^{-1}$ , and the horizontal map shows the same gradual decrease towards east, with the highest  
482 concentrations in the westernmost regions and minimum values in the eastern regions ( $< 0.25 \mu\text{mol kg}^{-1}$ ).  
483

484 The average vertical profile over the entire region (Fig. 9b10b), reveals a maximum in phosphate  
485 concentrations between 300 and 800 m depth, related to an increased remineralization process.

486 In the deep layer (see 1500 m, Fig. 8h9h), phosphate concentration average is  $0.36 \pm 0.02 \mu\text{mol kg}^{-1}$ .  
487 Generally, the deep layer is homogeneous (Fig. 9b10b). The difference observed between westernmost  
488 regions and the Tyrrhenian Sea remains, though the latter demonstrate higher phosphate concentrations  
489 ( $\sim 0.3 \mu\text{mol kg}^{-1}$ ). This variation could be due to the difference in the water masses. The IW inflow from  
490 the EMED brings relatively young waters that are depleted in nutrients, while in the higher  
491 concentrations in the deep layer are signatures of the older resident DW of the Tyrrhenian. The change  
492 in the biological uptake in the intermediate source water could explain the regional variability of  
493 nutrients. The low productivity (D'Ortenzio and Ribera d'Alcalà, 2009) and the pronounced  
494 oligotrophic regime of EMED water (Lazzari et al., 2016) may justify the increase in nutrients in the  
495 IW.

496 Silicate concentration distribution at intermediate (300 m, Fig. 8f9f) and deep layers (1500 m, Fig. 8i9i),  
497 were as expected, showing a notable increase, compared to the surface. Here the silicate average  
498 concentration is  $5.83 \pm 0.66 \mu\text{mol kg}^{-1}$ . The maximum values were observed below 800 m,  $> 8.034 \mu\text{mol}$   
499  $\text{kg}^{-1}$  (Fig. 4-9e10c). At 1500 m, silicate distribution is homogeneous all over the basin (on average  $8.35$   
500  $\pm 0.39$ ).

501 Generally, primary producers do not require silicate for their growth as much as they need nitrate and  
502 phosphate which explain the disparity between nutrients patterns. Furthermore, at intermediate levels,  
503 the water is warmer than at deep levels, enhancing the dissolution rate and the progressive increase in  
504 silicate (DeMaster, 2002). The biogenic silicate is exported to greater depths and continues to dissolve  
505 generating inorganic silicate as it sinks to the bottom. The recycling of silicate within the deep-sea  
506 sediments is later on redistributed by the deep currents which explain the homogenous horizontal  
507 distribution over the entire basin.

508 Comparing the three nutrients at the same depth levels, at the surface (100 m), it appears that they all  
509 show local surface maximum, depending on local events such as strong winds, local river discharge and  
510 vertical mixing (Ludwig et al., 2010).

511 In the easternmost areas, the surface depletion in nutrients (Van Cappellen et al., 2014) is attributed to  
512 the variation in the thermohaline properties that has impacted primary production (Ozer et al., 2017) and

513 the export of organic matter to intermediate and deep layers leading to the accumulation of nutrients in  
514 these depth ranges.

515 The Tyrrhenian Sea is not directly connected to convection regions. Here, the EMED water inflow  
516 plays a major role. Li and Tanhua (2020) found an increased ventilation of the intermediate and deep  
517 layers during 2001 to 2018 in the Sicily channel and a constant AOU between 2001-2016, suggesting a  
518 constant ventilation that explains the peculiar nutrient distribution in that area. In the western side of  
519 the WMED, intermediate and deep layers exhibit an increase in nutrients. Schroeder et al. (2020)  
520 explained this increase in nitrate and phosphate at the intermediate layer with the increase of the  
521 remineralization rate at these depths along the path of IW.

522 The deficiency of inorganic nutrients is explained by the effect of the anti-estuarine circulation, with the  
523 IW coming from the EMED, which is known to be poor in nutrients (Krom et al., 2014; Schroeder et  
524 al., 2020), accumulates nutrient along its path. Thus, this relative nutrient-rich Mediterranean outflow is  
525 lost to the Atlantic Ocean.

526 Overall, in surface layer, circulation, physical processes, and vertical mixing increase nutrient input  
527 while the biological pump controls the decrease.

528 In the deep layer, the variability is lower (standard deviation is reduced toward the bottom for all three  
529 nutrients, see Fig.9-10), the deep layer accumulates dissolved organic nutrients. In the WMED, the deep  
530 layer constitutes a reservoir of inorganic nutrients.

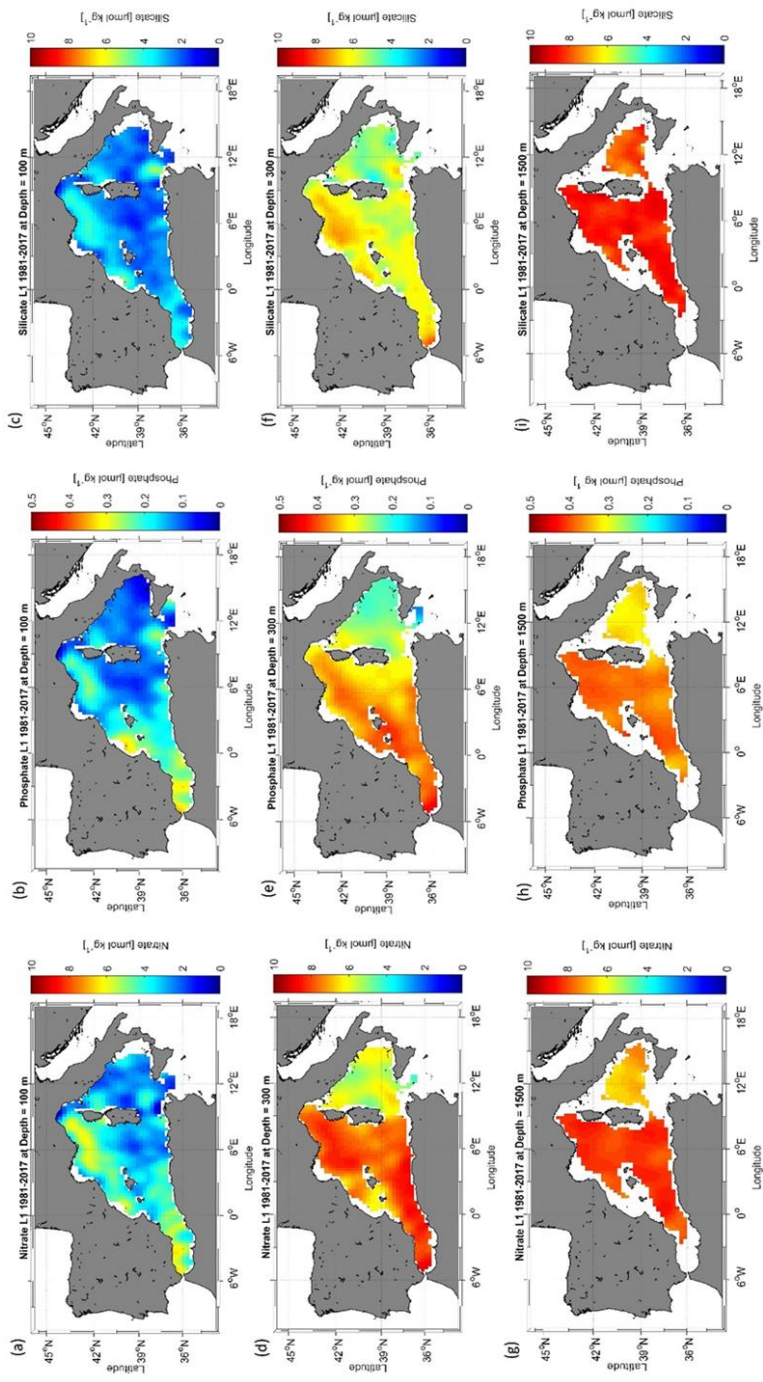
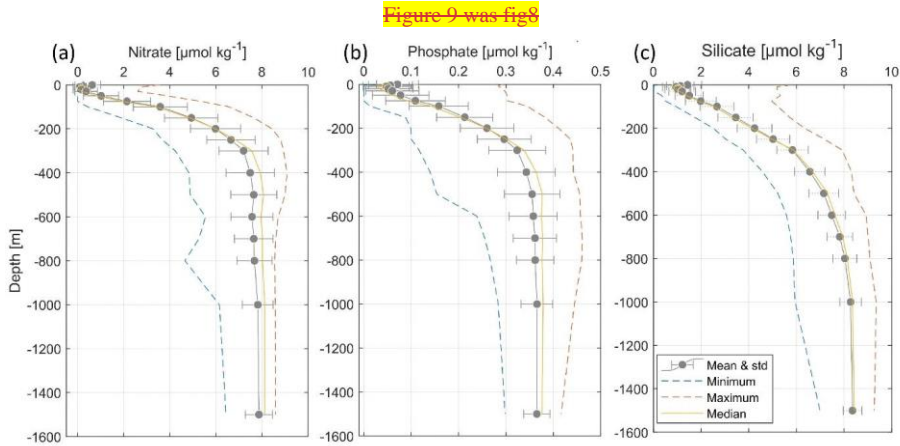


**Figure 99.** Climatological map distribution of nitrate (a. at 100 m, d. at 300 m, g. at 1500 m), phosphate (a. at 100 m, d. at 300 m, g. at 1500 m) and silicate (a. at 100 m, d. at 300 m, g. at 1500 m) for the period from 1981 to 2017.

Formatted: Not Highlight

Formatted: Not Highlight

531



532

533 **Figure 109.** Climatological mean vertical profiles of (a) nitrate, (b) phosphate and (c) silicate  
534 concentrations in the WMED (1981-2017). Dashed blue line indicates the minimum, dashed orange line  
535 indicates the maximum, continuous yellow line indicates median profile, error bars and mean profile are  
536 in grey.

#### 537 4.2 Error fields

538 The determination of the error field is important to gain insight in the confidence in the climatological  
539 results. Mostly, the error estimate depends on the spatial distribution of the observations and the  
540 measurement noise. In DIVAnd, there are different methods available to estimate the relative error  
541 associated with the analysis fields.

542 A climatological field is computed at several depths (19 levels in this case), for different parameters  
543 (nitrate, phosphate, and silicate in this case). Given these premises and following the approach of similar  
544 climatologies (GLODAPv2.2016b, Lauvset et al., 2016; SeaDataNet aggregated data sets products,  
545 Simoncelli et al., 2015), for the BCG-WMED the error fields were estimated using the default DIVAnd  
546 method, i.e. the “clever poor man’s error approach”, a less time consuming but efficient computational  
547 approach. According to Beckers et al. (2014) who also provides details about the mathematical  
548 background of the error fields computation, this method appropriately represents the true error and  
549 provides a qualitative distribution of the error estimate. This estimate is used to generate a mask over  
550 the analysis fields. Two error thresholds were applied (0.3 (L1) and 0.5 (L2)). Fig. 7b8b., show the main  
551 error that occurs in regions void from measurements. An example of the analysis masked with the error  
552 thresholds output is shown in Fig. 78c (L1) and Fig. 7d-8d (L2). The associated error fields with the  
553 analysis fields are integrated in the data product.

554 4.3 Comparison with other biogeochemical data products

555 In this section a comparison of the BGC-WMED product with the most known global and/or regional  
556 climatologies, that are frequently used as reference products for initializing numerical models, is  
557 ~~done~~.

558 Specifically, the analyzed fields are compared to the reference data products WOA18 (Garcia et al.,  
559 2019), ~~a large scale illustration of nutrient distribution and computed by objective analysis using the~~  
560 ~~World Ocean Database 2018 (Boyer et al., 2018). The new product is also compared to~~ the reanalysis  
561 of the Mediterranean Sea biogeochemistry, medBFM, a CMEMS product ~~that assimilates satellite and~~  
562 ~~Argo data and includes terrestrial inputs of nitrate and phosphate from 39 rivers~~ (Teruzzi et al., 2019).

563 Since the products used for inter-comparison were not originated from the same interpolation method,  
564 not for the same time period and with different spatial resolution, here the comparison is mostly targeted  
565 on the general patterns of nutrients in the region.

566 Comparisons are carried out between horizontal maps (Fig. ~~1011-1112-1213~~), as well as along a vertical  
567 longitudinal transect (Fig. ~~1415-1516~~). In addition, following Reale et al. (2020), the first 150 m have  
568 been evaluated (Fig. ~~1314~~), since this is a depth level with a representative amount of in situ observations  
569 in all three products. The evaluation is based on the estimation of horizontal average, on BGC-WMED  
570 climatology, the medBFM biogeochemical reanalysis and the WOA18 climatology by subregion. i.e. a  
571 spatial subdivision made according to Manca et al. (2004).

572 Products have a different grid resolution, thus to compare ~~between them and combine variables on a~~  
573 ~~compatible grid~~, the BGC-WMED new climatological data product (at  $0.25^\circ \times 0.25^\circ$ ) for ~~the~~ periods  
574 1981-2017, ~~and~~ 2005- 2017 and the medBFM biogeochemical reanalysis (at  $0.063^\circ \times 0.063^\circ$ ) (Teruzzi  
575 et al. 2019) ([https://doi.org/10.25423/MEDSEA\\_REANALYSIS\\_BIO\\_006\\_008](https://doi.org/10.25423/MEDSEA_REANALYSIS_BIO_006_008)) for the period 2005-  
576 2017, are regridded on the WOA18 ( $1^\circ \times 1^\circ$ ) grid ~~using nearest neighbor interpolation, changing the~~  
577 ~~resolution, of the existing grid to facilitate the comparison of the transect from each product.~~

578 The regridding is computed at all depth levels of the different products ~~using nearest neighbor~~  
579 ~~interpolation. Prior to the interpolation, the MedBFM-medBFM reanalysis of nitrate and phosphate~~  
580 ~~have been averaged across climatological mean was computed for the period 2005-2017 prior the~~  
581 ~~interpolation.~~

582 ~~We then calculated spatial maps of the mean difference at 150 m between the new climatology and the~~  
583 ~~reference products and then an average across subregions was performed.~~

Formatted: Font: (Default) Times New Roman, 11 pt, Font color: Auto, Complex Script Font: Times New Roman, 11 pt

Formatted: Font: (Default) Times New Roman, 11 pt, Font color: Auto, Complex Script Font: Times New Roman, 11 pt

Formatted: Font: (Default) Times New Roman, 11 pt, Font color: Auto, Complex Script Font: Times New Roman, 11 pt

Formatted: Font: (Default) Times New Roman, 11 pt, Font color: Auto, Complex Script Font: Times New Roman, 11 pt



584 4.3.1 Comparison with WOA18 at 150 m

585 Fig. 1011-124-132 show the analysis at the 150 m depth surface for the three nutrients. The BGC-  
586 WMED (1981-2017) product reveals detailed aspects of the general features of nitrate (Fig. 110.a),  
587 phosphate (Fig. 124a) and silicate (Fig.132a).

588 For the three nutrients, the new product reproduces patterns similar to the WOA18 all over the region.  
589 It shows well-defined fields and higher values of nitrate and phosphate concentrations. In the new  
590 product, nitrate concentrations varied between 2.31 -7.3  $\mu\text{mol kg}^{-1}$  the WOA18 values were 2.19 - 5.99  
591  $\mu\text{mol kg}^{-1}$ . Phosphate ranges were similar between the two products between (0.092- 0.35  $\mu\text{mol kg}^{-1}$   
592 (BGC-WMED) and 0.095 - 0.35  $\mu\text{mol kg}^{-1}$  (WOA18)). Likewise, Silicate range values at 150 m were  
593 not different (2.07 - 4.99 (BGC-WMED) and 1.57 - 5.75  $\mu\text{mol kg}^{-1}$ (WOA18)).

594 The average RMS difference (RMSD) calculated from the difference between the WOA18 and BGC-  
595 WMED all over the region at 150 m is about 1.14  $\mu\text{mol kg}^{-1}$  nitrate (Fig. 110c), 0.055  $\mu\text{mol kg}^{-1}$  for  
596 phosphate (Fig. 124c) and 0.91  $\mu\text{mol kg}^{-1}$  for silicate (Fig. 132c). Overall, the RMS error values were  
597 low indicating limited disparity between the two products.

598 The difference field for every grid point reflects this discrepancy and shows areas with limited  
599 agreement between the two products; that can have a difference  $>2 \mu\text{mol kg}^{-1}$  for nitrate (Fig. 110c),  
600  $>0.1 \mu\text{mol kg}^{-1}$  for phosphate (Fig. 124c),  $>1.5 \mu\text{mol kg}^{-1}$  for silicate (Fig. 132c). This dissimilarity is also  
601 noted with the low  $r^2$  (Fig. 143) (0.34, 0.20, 0.095 for nitrate, phosphate, and silicate respectively)

602 The distribution of the surface nitrate concentrations (at 150 m) (Fig. 110a) of the new product is similar  
603 to that shown in WOA18 (Fig. 110b). The largest difference between the two products occurs in  
604 northwest areas and in the Alboran Sea (Fig. 110c), areas of higher concentrations, a more nutrient rich  
605 surface water as described in section 4.1. The difference is pronounced in these regions likely because  
606 of the occurrence of upwellings along the African coast and seasonal vertical mixing in the northern  
607 WMED, contributing to the upload of nutrients to the surface which could explain the high nitrate and  
608 phosphate concentration in the BGC-WMED. The WOA18 maps show weaker values of nutrient  
609 concentrations compared to the new product which does not mean that there are fewer physical drivers,  
610 but it might indicate that the new product holds more in situ observations than the WOA18 in the  
611 WMED.

612 Phosphate surface concentrations (Fig. 124) show similar differences as nitrate. The largest difference  
613 with the surface phosphate of the WOA18 is found in the Alboran Sea, Northern WMED and Sicily  
614 region (Fig. 124c).

615 As for silicate, the surface distribution shows large differences (Fig. 124e13c). The highest values are  
616 observed in the northwest area of the new product, and in the Alboran Sea in the WOA18 climatology ,  
617 this again accounts for the data coverage difference.

Formatted: Not Highlight

Formatted: Not Highlight

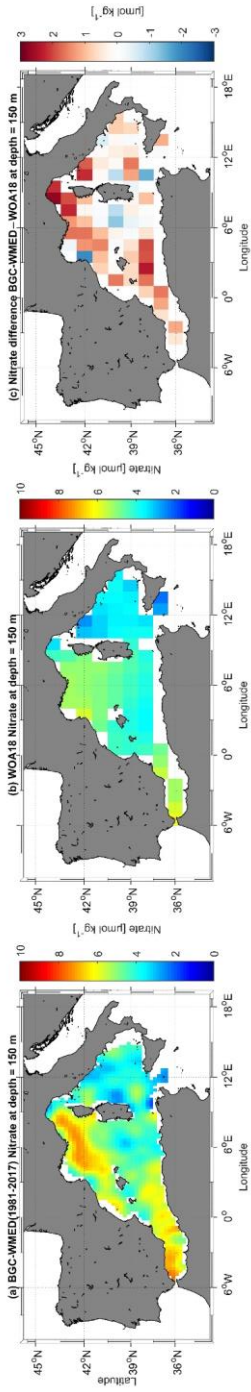


**Figure 11.** (a) BGC-WMED (1981-2017) Nitrate climatological field at 150 m depth; (b) WOA18 nitrate climatological field at 150 m depth; (c) difference between BGC-WMED and WOA18 nitrate fields at 150 m.

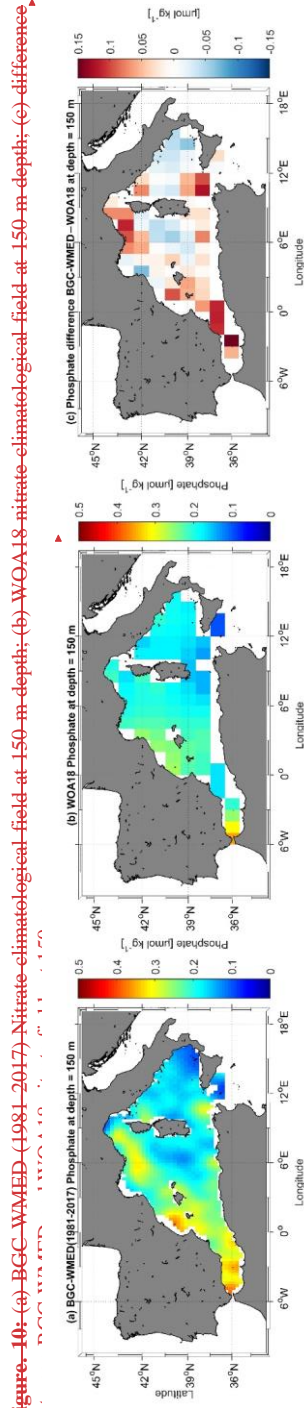


**Figure 12.** The same as Fig. 11 but for Phosphate.

**Figure 11.** The same as Fig. 4.10 but for Phosphate.

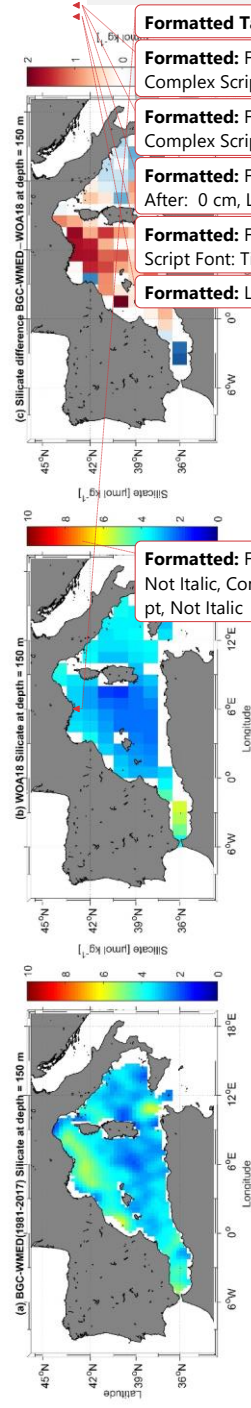


**Figure 13.** The same as Fig. 11 but for Silicate.

**Figure 12.** The same as Fig. 4.10 but for Silicate.

**Formatted Table**

**Formatted:** Font: (Default) Times New Roman, 11 pt, Complex Script Font: Times New Roman, 11 pt

**Formatted:** Font: (Default) Times New Roman, 11 pt, Complex Script Font: Times New Roman, 11 pt

**Formatted:** Figure Heading, Indent: Before: 0 cm, After: 0 cm, Line spacing: single

**Formatted:** Font: (Default) Times New Roman, Complex Script Font: Times New Roman

**Formatted:** Left

**Formatted:** Font: (Default) Times New Roman, 11 pt, Not Italic, Complex Script Font: Times New Roman, 11 pt, Not Italic

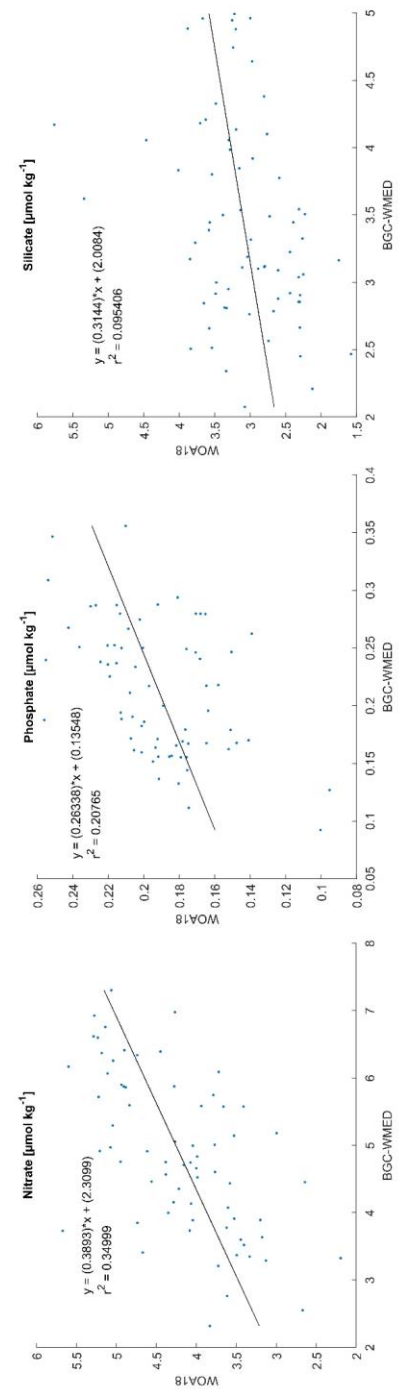


**Figure 14.** Scatterplot showing the WOA18 data as a function of the BGC-WMED climatology at 150 m with the regression line.

Formatted: English (United States)

Field Code Changed

Formatted: English (United States)

618 4.3.2 Regional horizontal comparison above 150 m average nutrient concentrations

619 The inorganic nutrient mean concentrations resulting from the climatology of this work (period 2005-  
620 2017), and from both the medBFM reanalysis product and the WOA18 are compared in the upper layer  
621 of 12 subregions of the WMED (in Table 4 and Fig. 154).

622 Results show a general agreement between BGC-WMED and the other two products in some  
623 subregions, nonetheless, there are some differences as shown in section 4.3.1.

624 Upper layer nitrate average concentrations (Fig. 14a15a) are decreasing eastward, from the Alboran Sea  
625 (DS1) to the Algerian basin (DS3, DS4) and the Balearic Sea (DS2). The western part of the basin is an  
626 area under the direct influence of the inflowing Atlantic surface waters, where nitrate is known to be  
627 present in excess compared to phosphate probably due to atmospheric N<sub>2</sub> input (Lucea et al., 2003). In  
628 the DS1, BGC-WMED nitrate levels are lower than the WOA18 nitrate levels while in DS3, DS2 and  
629 DS4 the average nitrate concentrations are similar to the WOA18.

630 From the Algerian basin (DS4, DF1) to Liguro-Provençal (DF3) regions, there is an increase in the  
631 average nitrate in all products, this is the south-north gradient. Some difference arises, where the new  
632 product is lower than the WOA18.

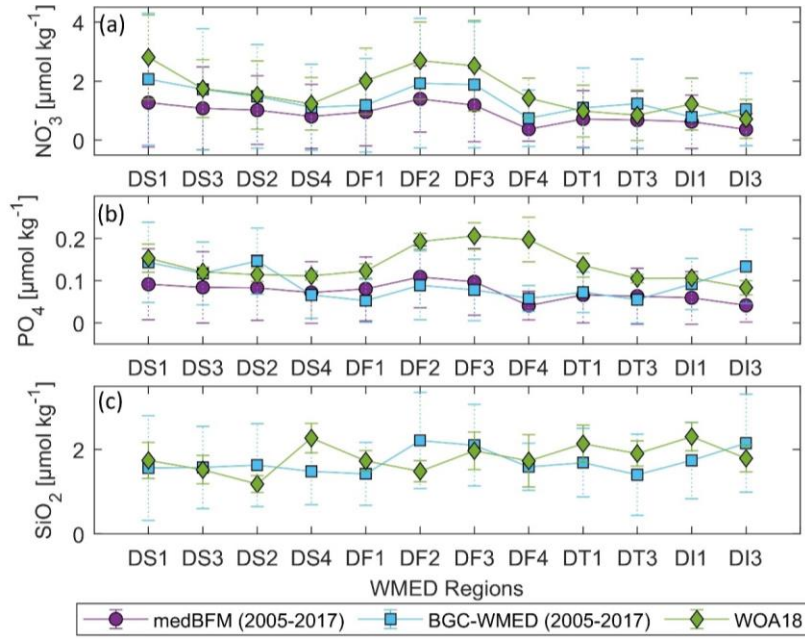
633 In the eastern regions, the lowest average concentrations of the WMED are found. Here, the difference  
634 between products is smaller, with medBFM reanalysis being lower than the new product and the  
635 WOA18.

636 As for phosphate (Fig. 154b), known to be the limiting nutrient of the WMED, because it is rapidly  
637 consumed by phytoplankton (Lucea et al., 2003), its average levels are low in DS1, DS3, DS2 and DS4,  
638 in WOA18, medBFM reanalysis and BGC-WMED. The latter did not agree well with the other products  
639 in DS2, where it was slightly higher. Phosphate average concentrations slightly increase in DF1, DF2  
640 and DF3 in all three products. The increase is explained by the vertical mixing process occurring in the  
641 northern WMED.

642 Upper surface phosphate concentrations average start to decrease progressively through the Ligurian  
643 East (DF4), Tyrrhenian Sea (DT1, DT3), Sardinia Channel (DI1) and Sicily Channel (DI3). The BGC-  
644 WMED was in agreement with medBFM reanalysis in those subregions aside from concentrations in  
645 DI3, where the new product showed higher levels.

646 The BGC-WMED climatology shows reasonable agreement in the upper average concentrations of  
647 nitrate and phosphate that are similar in order of magnitude to the other products (Fig. 154). The  
648 difference with the WOA18 resides in the wider temporal window of the observation (starting from  
649 1955). The new climatology in some subregions has a better spatial coverage of in situ observation than  
650 the WOA18 (Garcia et al., 2019) and the medBFM reanalysis (Teruzzi et al., 2019).

651 On the other hand, the average silicate (Fig. 154c) of the new product and the WOA18 varied between  
 652 regions. Significant difference is found between the two products in DS2, DS4, DF1, DF2, DT1, DT3,  
 653 DI1 and DI3, while in DS1, DS3 and DF4 mean silicate is consistent between the two products.  
 654 Overall, the three products show strongly similar features between regions (similar curve shape).



655  
 656 **Figure 154.** Nutrient average concentrations and standard deviation comparison in the upper 150 m  
 657 (values in Table 4).

658  
 659  
 660  
 661  
 662  
 663  
 664  
 665  
 666

667 **Table 4.** Nutrient average concentrations and standard deviation in the upper 150 m. All products were  
 668 interpolated on 1° grid resolution (see Figure S2 (Belgacem et al., 2020)).

Subregion/ Coverage	Data product	Nitrate	Phosphate	Silicate
<i>DS1- Alboran Sea</i> (35°N– 37.3°N, -6°E– -1°E)	medBFM	1.27(±1.4)	0.09(±0.08)	-
	BGC-WMED	2.06(±2.2)	0.14(±0.09)	1.56(±1.2)
	WOA18	2.81(±1.4)	0.15(±0.03)	1.74(±0.4)
<i>DS3- Algerian West</i> (35.36°N– 38.3°N, -1°E– 4.3°E)	medBFM	1.07(±1.4)	0.08(±0.08)	-
	BGC-WMED	1.72(±2.05)	0.11(±0.07)	1.57(±0.9)
	WOA18	1.74(±0.9)	0.12(±0.01)	1.52(±0.3)
<i>DS2- Balearic Sea</i> (38.3°N– 42°N, -1°E–4.3 °E)	medBFM	1.02(±1.1)	0.08(±0.07)	-
	BGC-WMED	1.48(±1.7)	0.14(±0.07)	1.63(±0.9)
	WOA18	1.53(±1.1)	0.11(±0.01)	1.18(±0.2)
<i>DS4- Algerian East</i> (36.3°N– 39.18°N, 4.3°E– 8.24°E)	medBFM	0.80(±1.08)	0.07(±0.07)	-
	BGC-WMED	1.11(±1.4)	0.06(±0.05)	1.48(±0.7)
	WOA18	1.23(±0.8)	0.11(±0.009)	2.27(±0.3)
<i>DF1- Algero-Provençal</i> (39.18°N– 41°N, 4.3°E– 9.18°E)	medBFM	0.96(±1.15)	0.08(±0.07)	-
	BGC-WMED	1.18(±1.5)	0.05(±0.05)	1.42(±0.7)
	WOA18	2.00(±1.1)	0.12(±0.01)	1.73(±0.2)
<i>DF2- Gulf of Lion</i> (42°N–43.36°N, 1°E–6.18°E)	medBFM	1.39(±1.19)	0.10(±0.07)	-
	BGC-WMED	1.92(±2.1)	0.08(±0.08)	2.21(±1.1)
	WOA18	2.68(±1.3)	0.19(±0.01)	1.48(±0.2)
<i>DF3- Liguro-Provençal</i> (41°N– 45°N, 6.18°E– 9.18°E)	medBFM	1.18(±1.2)	0.09(±0.07)	-
	BGC-WMED	1.88(±2.1)	0.07(±0.07)	2.10(±0.9)
	WOA18	2.52(±1.5)	0.20(±0.03)	1.97(±0.4)
<i>DF4- Ligurian East</i> (42.48°N–45°N, 9.18°E– 11°E)	medBFM	0.37(±0.4)	0.04(±0.03)	-
	BGC-WMED	0.74(±0.9)	0.05(±0.03)	1.59(±0.5)
	WOA18	1.42(±0.6)	0.19(±0.05)	1.73(±0.6)
<i>DT1- Tyrrhenian North</i> (39.18°N–42.48°N, 9.18°E– 16.16°E)	medBFM	0.71(±0.9)	0.06(±0.06)	-
	BGC-WMED	1.09(±1.3)	0.07(±0.04)	1.69(±0.8)
	WOA18	0.98(±0.8)	0.13(±0.02)	2.13(±0.4)
<i>DT3- Tyrrhenian South</i> (38°N– 39.18°N, 10°E– 16.16°E)	medBFM	0.68(±0.96)	0.06(±0.06)	-
	BGC-WMED	1.23(±1.5)	0.05(±0.05)	1.40(±0.9)
	WOA18	0.84(±0.8)	0.10(±0.01)	1.90(±0.2)
<i>DII- Sardinia Channel</i> (36°N– 39.18°N, 8.24°E– 10°E)	medBFM	0.62(±0.9)	0.05(±0.06)	-
	BGC-WMED	0.78(±1.3)	0.09(±0.06)	1.74(±0.9)
	WOA18	1.22(±0.8)	0.10(±0.007)	2.3(±0.30)
<i>DI3- Sicily Channel</i> (35°N– 38°N, 10°E–15°E)	medBFM	0.36(±0.5)	0.04(±0.03)	-
	BGC-WMED	1.04(±1.2)	0.13(±0.08)	2.15(±1.1)
	WOA18	0.72(±0.6)	0.08(±0.01)	1.79(±0.3)

669 4.3.3 Regional vertical comparison of nitrate and phosphate concentrations

670 As the last step in the comparison between the different products, it is investigated how the new  
 671 climatology represents the vertical distribution by comparing the new climatological values for the  
 672 period 2005-2017 with the medBFM reanalysis and the WOA18.

673 We extracted data values along a longitudinal transect across the Algerian basin in the west-east  
 674 direction (Fig. [4516](#)). The transect was selected according to previous studies (D’Ortenzio and Ribera

675 d'Alcalà, 2009; Lazzari et al., 2012; Reale et al., 2020) and since the Easternmost part of the domain is  
676 showing markedly features, a transect across the Tyrrhenian Sea is extracted as well (Fig. 4516). Silicate  
677 is not included as it was not represented in the medBFM model.

678 Vertical sections of nitrate and phosphate in the Algerian Sea show a common agreement between  
679 products about the main patterns found along the water column, i.e. the nutrient depleted surface layer  
680 and the gradual increase toward intermediate depths, we note as well the west to east decreasing gradient  
681 in the three products, yet, there are some inequalities.

682 Below 100 m, there is a significant difference between products and a poor qualitative agreement.  
683 Nitrate distribution is dominated by the nutrient enriched IW, with high values ( $>7 \mu\text{mol kg}^{-1}$ ) increasing  
684 from east to west (Fig. 4516). Phosphate shows similar patterns in the surface layer, exhibiting very low  
685 concentration in the surface layer and a progressive increase down to 300 m ( $> 0.35 \mu\text{mol kg}^{-1}$ ) noted  
686 also in the WOA18. The reanalysis showed a more smoothed field, below 100-300 m, with phosphate  
687 concentration between 0.20 and  $0.30 \mu\text{mol kg}^{-1}$ . The highest values for phosphate were found below 250  
688 m from  $0^{\circ}\text{E}$  to  $3^{\circ}\text{E}$  in the new product. The BGC-WMED transect define very well the different depth  
689 layers, the upper intermediate layer is rich with nutrient concentration with  $> 8 \mu\text{mol kg}^{-1}$  for nitrate  
690 (BGC-WMED) and  $>0.35 \mu\text{mol kg}^{-1}$  for phosphate (BGC-WMED and WOA18).

691 The vertical section along the Tyrrhenian Sea (Fig. 4516) also shows a decrease from west to east in  
692 nitrate concentrations. The same gradient is found also in phosphate in agreement with nutrient  
693 distribution shown from the WOA18. From the section of the medBFM reanalysis, it is not easy to  
694 identify the west-east gradient that we mentioned before. It could be suggested that the model under-  
695 estimate the vertical features in the Eastern (Tyrrhenian Sea: 100-300 m, nitrate vary between 1.4 and  
696  $4.2 \mu\text{mol kg}^{-1}$ , phosphate between 0.13 and  $0.20 \mu\text{mol kg}^{-1}$ ) and western part (Algerian basin: 100-300  
697 m, nitrate vary between 2.1 and  $5.4 \mu\text{mol kg}^{-1}$ , phosphate between 0.15 and  $0.255 \mu\text{mol kg}^{-1}$ ). These  
698 values are lower than the ones found in the BGC-WMED (Tyrrhenian Sea: 100-300 m, nitrate range  
699 between 3 to  $6 \mu\text{mol kg}^{-1}$ , as for phosphate values oscillate between 0.10- $0.27 \mu\text{mol kg}^{-1}$ ; Algerian basin:  
700 100-300 m, nitrate range between 3.6 to  $8 \mu\text{mol kg}^{-1}$ , as for phosphate values oscillate between 0.18-  
701  $0.36 \mu\text{mol kg}^{-1}$ ).

702 While the WOA18 reproduce similar patterns as the new climatology (Tyrrhenian Sea: 100-300 m,  
703 nitrate vary between 1.8 and  $5.7 \mu\text{mol kg}^{-1}$ , phosphate between 0.33 and  $0.20 \mu\text{mol kg}^{-1}$ ) and western  
704 part (Algerian basin: 100-300 m, nitrate vary between 2.8 and  $6.8 \mu\text{mol kg}^{-1}$ , phosphate between 0.16  
705 and  $0.34 \mu\text{mol kg}^{-1}$ ).

706 The products illustrate the nutrient-poor water in the eastern side (Tyrrhenian Sea) and the relatively  
707 nutrient-rich water found in the western transect (Algerian basin).

708 The BGC-WMED product capture details in Fig. ~~15-16~~ about the longitudinal gradient in nitrate and  
709 phosphate, along the water column where nutrient sink deeper from west to east as previously seen in  
710 Pujo-Pay et al. (2011) and Krom et al. (2014), an increased oligotrophy from west to east with higher  
711 concentrations in the two nutrients in the western side of the section and a more oligotrophic character  
712 toward east.

713 The differences between products could be explained by the difference in the data coverage, time span  
714 and the difference in methods used to construct the climatological fields.

715 The variability in nitrate and phosphate fields along the transect extracted from the BGC-WMED reflects  
716 the high resolution of the product allowing the screening of vertical structure controlling nutrient  
717 contents. Based on a visual comparison, the new product is able to reproduce similar patterns as to the  
718 WOA18 and to a lesser ~~extend extent~~ the medBFM reanalysis.

719 Fig. ~~16-17~~ examines the vertical difference of nitrate and phosphate concentration for the BGC-WMED  
720 with the medBFM reanalysis along the Algerian basin (Fig. ~~16a-17a~~, nitrate; Fig. ~~16b-17b~~, phosphate) and  
721 WOA18 (Fig. ~~16e-17c~~, nitrate; Fig. ~~16d-17d~~, phosphate).

722 The vertical section shows a strong agreement at the surface for nitrate between the BGC-WMED and  
723 the medBFM reanalysis (Fig. ~~17-16a~~), while the vertical difference with WOA18 demonstrates that  
724 nitrate values in the new product are lower than the WOA18 at 50- 75 m (Fig. ~~16e-17c~~).

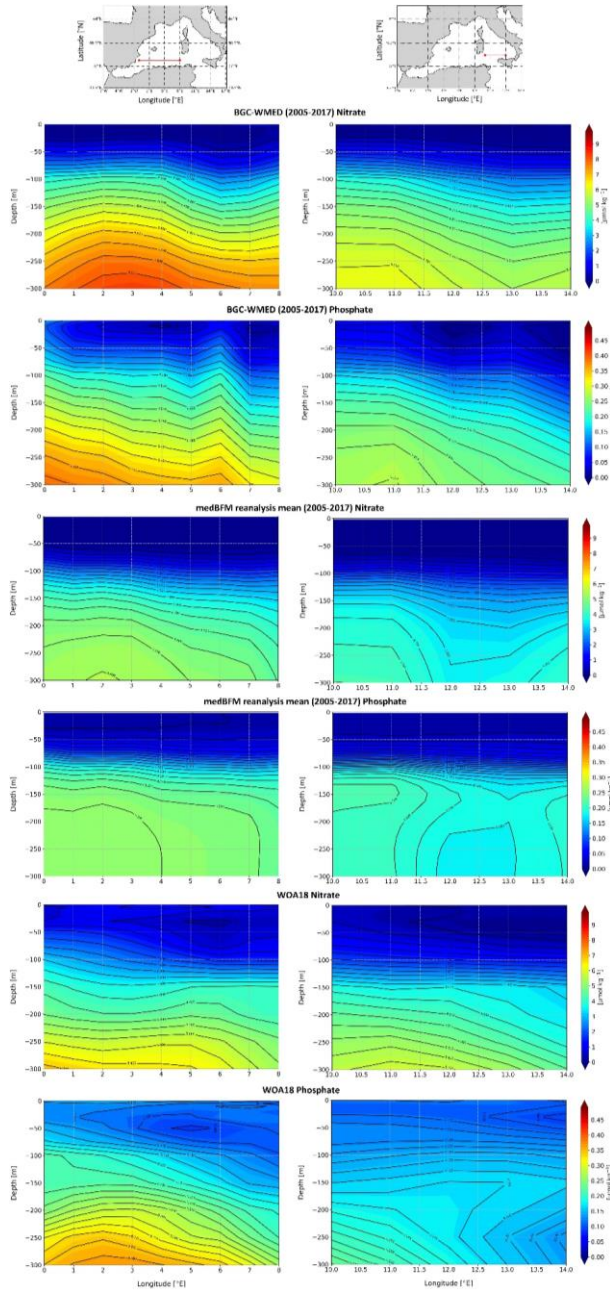
725 The difference increases with depth, below 100 m, the BGC-WMED nitrate climatology is higher than  
726 the medBFM with a difference ranging between 0.6 and 2.4  $\mu\text{mol kg}^{-1}$ , similar observation is noted in  
727 the WOA18 (Fig. ~~16e-17c~~). In Fig. ~~16a-17a~~ and Fig. ~~16e-17c~~, we identify patterns in the vertical structure  
728 of nitrate in the eaten portion of the transect.

729 Regarding phosphate, differences between the new climatology and the medBFM reanalysis are noted  
730 (Fig. ~~16b-17b~~) where the BGC-WMED shows high concentrations in the first 100 m and between 150 m  
731 and 300 m (differences of 0.02 - 0.08  $\mu\text{mol kg}^{-1}$ ), this difference decreases at 100-150 m. At the eastern  
732 portion of the transect (6°E to 7.5°E), we find an agreement between the two products.

733 Conversely, the vertical sections of the differences between BGC-WMED and WOA18 in phosphate  
734 (Fig. ~~16-17 d~~) show similarities, with the new product being lower than the WOA18 in the first 50 m.  
735 Large difference is found on both sides of the transect below 100 m, while in the center of the transect,  
736 the difference in phosphate is reduced to 0-0.02  $\mu\text{mol kg}^{-1}$ .

737 Fig. ~~17-18~~ compares the vertical difference of nitrate and phosphate along the Tyrrhenian Sea transect.  
738 In general, the difference transect in the Tyrrhenian Sea shows similar features with medBFM reanalysis  
739 and the WOA18 as in Algerian basin. Fig. ~~17d-18d~~ captures the west to east gradient in phosphate. The  
740 WOA18 overestimated phosphate in the surface layer.



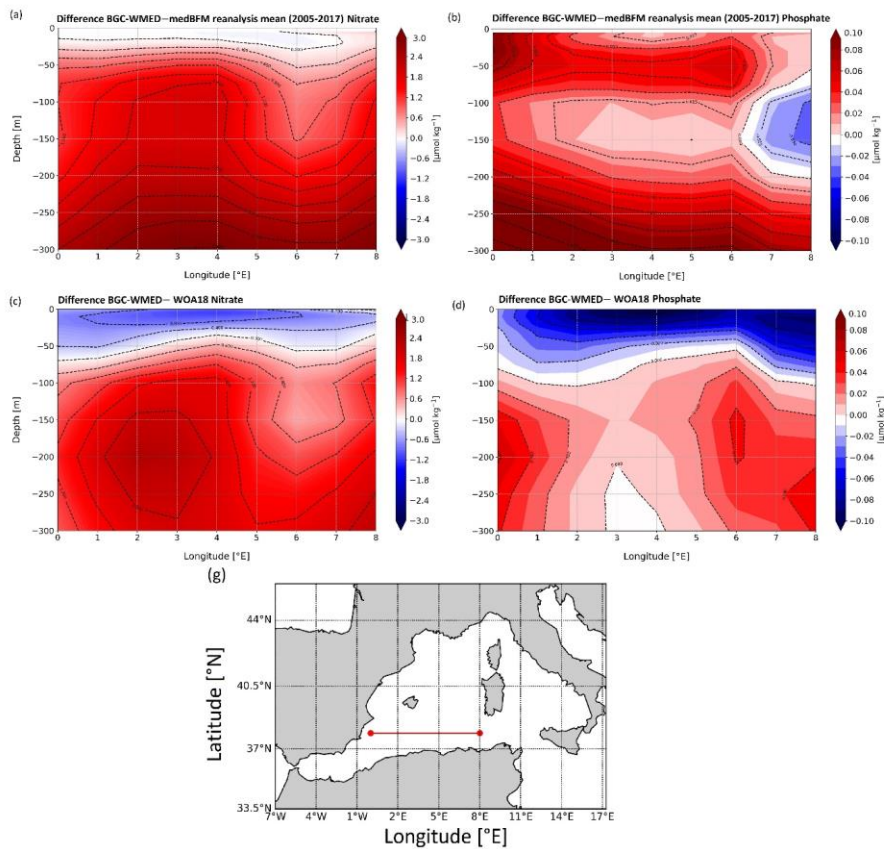


742 **Figure 1615.** Vertical distribution of nitrate and phosphate from the Algerian basin and Tyrrhenian Sea.  
743 Colors show the gridded values from the three different products: BGC-WMED, medBFM reanalysis  
744 (Teruzzi et al.,2019) and the WOA18 (Garcia et al., 2019).

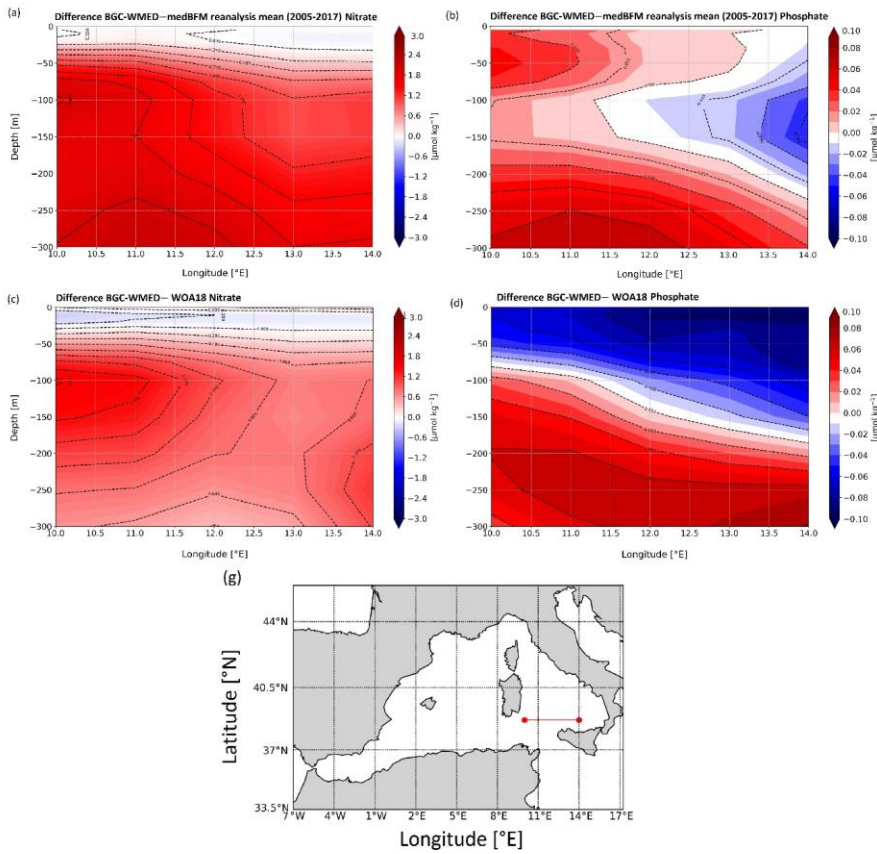
745 Based on the new climatology comparison with the WOA18 and the reanalysis, it is concluded that the  
746 new product is consistent with the main features of previous products and show the large-scale patterns  
747 and underline well the characteristics of the water mass layers.

748 The study also provides an examination of the nitrate and phosphate distributions along a longitudinal  
749 transect across the Algerian Basin (Western WMED) and across the Tyrrhenian Sea (Eastern WMED).

750 We have shown that the western basin is relatively high in nutrients compared to the Eastern basin. The  
751 increased oligotrophic gradient from west to east could be attributed to the difference in the  
752 hydrodynamic patterns related to the water mass specific properties that are affected by the EMED and  
753 the Atlantic ocean inflows, and to the local sources of nutrients (Ribera d'Alcalà et al., 2003; Schroeder  
754 et al., 2010). Study of Crispi et al. (2001) inferred ~~to~~ the biological activity that is responsible for the  
755 oligotrophic gradient.



756  
 757 **Figure 1746.** Difference of vertical section from the Algerian basin between BGC-WMED and  
 758 medBFM (a. nitrate, b. phosphate), BGC-WMED and WOA18 (c. nitrate, d. phosphate), with dashed  
 759 contour lines and labels.



760

761 **Figure 18** ~~Figure 17~~. Same as Fig. ~~16-17~~ but for the vertical section from the Tyrrhenian Sea.

**Formatted:** Font: Bold, Complex Script Font: Bold

**Formatted:** Font: Bold, Complex Script Font: Bold

762 4.4 Temporal comparison: 1981-2004 vs 2005-2017

763 In this section, we compare between two climatological periods (1981-2004 vs 2005-2017). The  
 764 distinction between the two period was based on the occurrence of the ~~western~~-Western Mediterranean  
 765 ~~transition~~-Transition (WMT) that started in 2004/05, during which there was a progressive increase in  
 766 temperature and salinity of the IW that led to important deep convection events, substantially increasing  
 767 the rate of DW formation between 2004 and 2005 (Schroeder et al., 2016).

768 The result of this climatological event was that a newly generated DW, denser, saltier, and warmer than  
 769 the old WMDW, filled up the WMED. The new WMDW propagated east toward the Tyrrhenian Sea  
 770 and west toward the Alboran Sea and Gibraltar (Schroeder et al., 2016).

771 A recent study of Li and Tanhua (2020) demonstrated an enhanced ventilation in the WMED deep layers  
 772 despite the continuous overall increase in temperature (Bindoff et al., 2007), salinity and density of

773 intermediate and deep layers after the WMT (Schroeder et al., 2016; Vargas-Yáñez, 2017). An increased  
774 ventilation means a DW renewal (Schroeder et al., 2016; Tanhua et al., 2013) subsequently a well  
775 oxygenated waters, implying an increase in the decomposition of the sinking organic matters into  
776 inorganic nutrients, thus causing changes of biogeochemical cycles (Shepherd et al., 2017). What  
777 happened in the WMED was not a permanent continuous event, since DW formation faded during the  
778 years 2006 and 2007, to restart again in 2008 (Li and Tanhua, 2020). In this section, we investigate the  
779 possible impact of WMT on biogeochemical characteristics at different depth levels (with a focus on  
780 nitrate, phosphate and silicate regional distribution and patterns).

781 We considered depth levels that represent the usual three layers: the surface (100 m; Fig. ~~18a19a-19a20a-~~  
782 ~~210a~~), intermediate (300 m; Fig. ~~18b19b-19b20b-20b21b~~) and deep layers (1500 m; Fig. ~~18e19c-2019c-~~  
783 ~~210c~~).

784 The WMED surface layer is dominated by the AW coming through the Alboran Sea, a permanent area  
785 of upwelling (García-Martínez et al., 2019), where there is a continuous input of elements from the layer  
786 below to the surface (Fig. ~~18a19a-19a20a-210a~~). Nitrate increased after WMT (Fig. ~~198d-2019d-210d~~)  
787 by  $+0.4137 \mu\text{mol kg}^{-1}$  (Fig. ~~A14S~~a). The largest difference between the two periods reached  $>+2 \mu\text{mol}$   
788  $\text{kg}^{-1}$  in Sardinia Channel and the Alboran Sea that was explained by the favorable conditions for nitrogen  
789 fixation as discussed in Rahav et al. (2013), revealing also that nitrogen fixation rate increased from  
790 east-to-west. Phosphate and silicate on the other hand described a decrease at 100 m (Fig. ~~S4aA4a~~) with  
791 about  $-0.021$  and  $-0.1365 \mu\text{mol kg}^{-1}$  ~~in-on~~ average, respectively. Large ~~changes~~ ~~is~~are noticed in the  
792 southern Alboran Sea, Sardinia channel and Balearic Sea.

793 The surface layer exhibits an irregular distribution since it is subjected to seasonal variability. We found  
794 ~~and~~ an increase in all nutrients at 300 and 1500 m with a maximum identified at intermediate depth in both  
795 nitrate and phosphate which is explained by the remineralization of organic matter along the path of the  
796 IW. The latter flows westward (from the Levantine to the Atlantic Ocean). Its content in nutrients  
797 increases (relatively to the conditions in the EMED) with age (Schroeder et al., 2020). It arrives ~~to-at~~ the  
798 Tyrrhenian Sea, where in Fig. ~~18b19b-19b20b-20b-21b~~ (at 300 m depth), we identify a nutrient-depleted  
799 intermediate layer. At this depth level, we observe a gain in the three nutrients after WMT (Fig. ~~18e19c-~~  
800 ~~19e20e-20e21e~~). ~~On~~ average, the difference between the two periods (pre/post-WMT) for nitrate,  
801 phosphate, and silicate, is around  $+0.8648$ ,  $+0.0068$  and  $+0.2072 \mu\text{mol kg}^{-1}$  (Fig. ~~S4bA4b~~), respectively.

802 A similar increase after WMT in the deep layer (1500 m), is also found for nutrient concentrations (Fig.  
803 ~~18f19f, 19f20f, 20f21f~~) in the magnitude of  $+0.753$  for nitrate,  $+0.025$  for phosphate, and  $+0.867$  for  
804 silicate (Fig. ~~S4eA4c~~), which highlights an increase in the downward flow of organic matter  
805 remineralization that is supplying the existing pool.

806  
807 This increase is also illustrated in the climatological mean vertical profile of Fig. ~~21-22~~ in the three  
808 nutrients. Nitrate displays a notable vertical difference to the pre-WMT period below 200 m (Fig.

809 ~~21a22a~~). Phosphate difference between the two-time period is larger below 400 m (Fig. ~~21b22b~~). Silicate  
810 was different ~~than-from~~ nitrate and phosphate. It increases progressively with depth (Fig. ~~20e22c~~) and  
811 demonstrates~~d~~ an enrichment of the DW compared to the 1981-2004 period (Fig. ~~21e21c~~). The  
812 maximum values are found in the deep layer, due to the low remineralization rate. With the warming  
813 climate, biogenic silicate~~e~~ tends to dissolve faster which explains~~s~~ the high concentrations all over the  
814 basin even the Tyrrhenian Sea after the WMT.

815 According to Stöven and Tanhua (2014), the impressive volume of the newly formed DW during 2004  
816 and 2006, ventilated the old DW decreasing its age, meaning that the WMT could have led to the  
817 lowering of the WMED deep layer pool in nutrient as it was pointed out by Schroeder et al. (2010).  
818 However, we did not observe this decrease in the climatological analysis after the WMT. It might be  
819 due to the temporal variability of the deep convection intensity, since a decrease has been recorded in  
820 the Gulf of Lion between 2007 and 2013 (Houpert et al., 2016).

821 A decrease in the deep convection intensity since the WMT (Houpert et al., 2016; Li and Tanhua, 2020),  
822 could potentially lead to the reduction in the supply from the nutrient-rich DW (before WMT) to the  
823 surface, i.e. the decrease in nutrient could have happened right after the WMT in spring 2005 where  
824 Schroeder et al. (2010) reported peculiar divergence between the old WMDW and the new WMDW in  
825 nitrate and phosphate; the new WMDW was low in nutrient; later on an intense DW formation event  
826 marked the year 2012 with a strong ventilation that has been recorded in the Adriatic Sea that could  
827 have affected the WMED. It was not possible to observe this change since we calculated the mean state  
828 of the basin spanning a specific period.

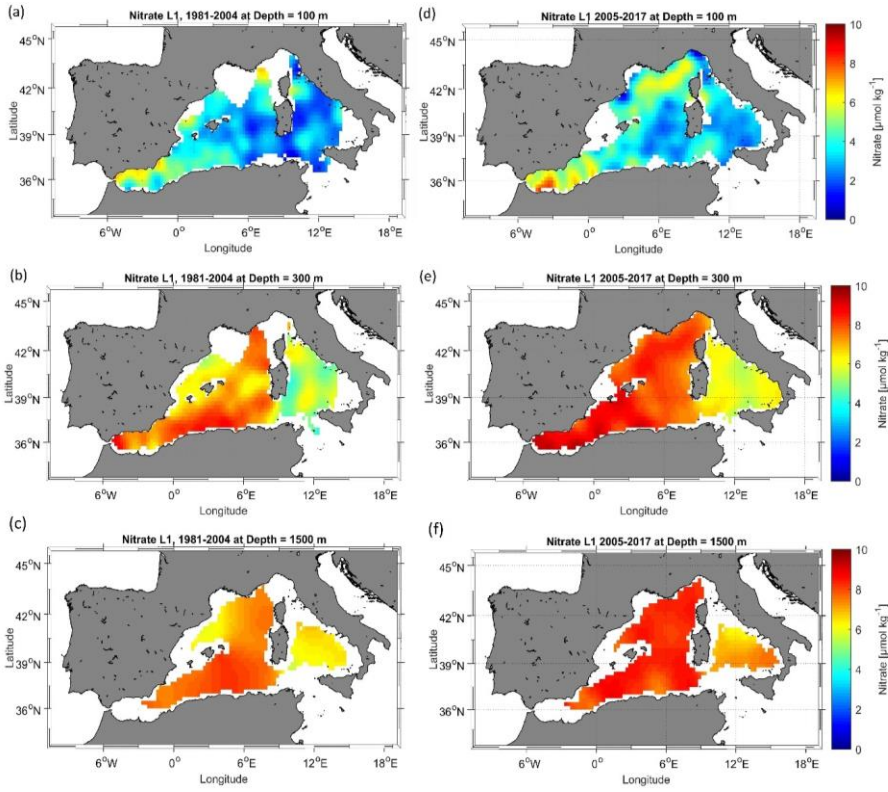
829 The spatial distribution of nutrient concentrations after the WMT (2005-2017) was quite different from  
830 the one before the WMT (1981-2004). This could also be related to the significant decline in river  
831 discharge between 1960 and 2000, ~~thawhich~~ was estimated to 20% (Ludwig et al., 2009). The decrease  
832 is also observed in silicate fluxes, since silicate loads through river discharge.

833 The change could be explained by the low denitrification rate for nitrate and an increase in the  
834 remineralization of organic matter. Though, Ludwig et al. (2009) reported an increase in nitrate and  
835 phosphate fluxes that was enhanced by the anthropogenic inputs (Ludwig et al., 2009), loading the deep  
836 layer with inorganic nutrients, also it could be associated with the slower ventilation of the WMED  
837 waters and a longer residence time.

Field Code Changed

Formatted: Not Highlight

Formatted: Not Highlight

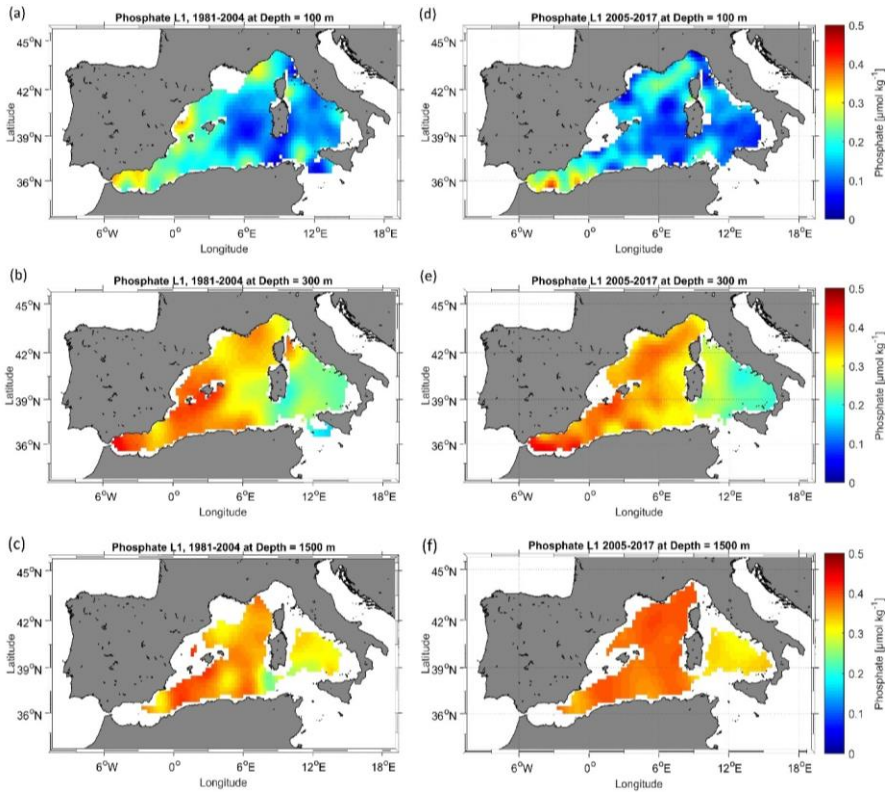


838  
 839 **Figure 19**Figure 18. Nitrate climatological field (masked analysis fields masked using relative error  
 840 threshold = 0.3 (L1)) at 100 m, 300 m, and 1500 m, for two periods: 1981-2004 (a, b, c) and 2005-2017  
 841 (d, e, f).

**Formatted:** Font: Bold, Complex Script Font: Bold

**Formatted:** Font: Bold, Complex Script Font: Bold





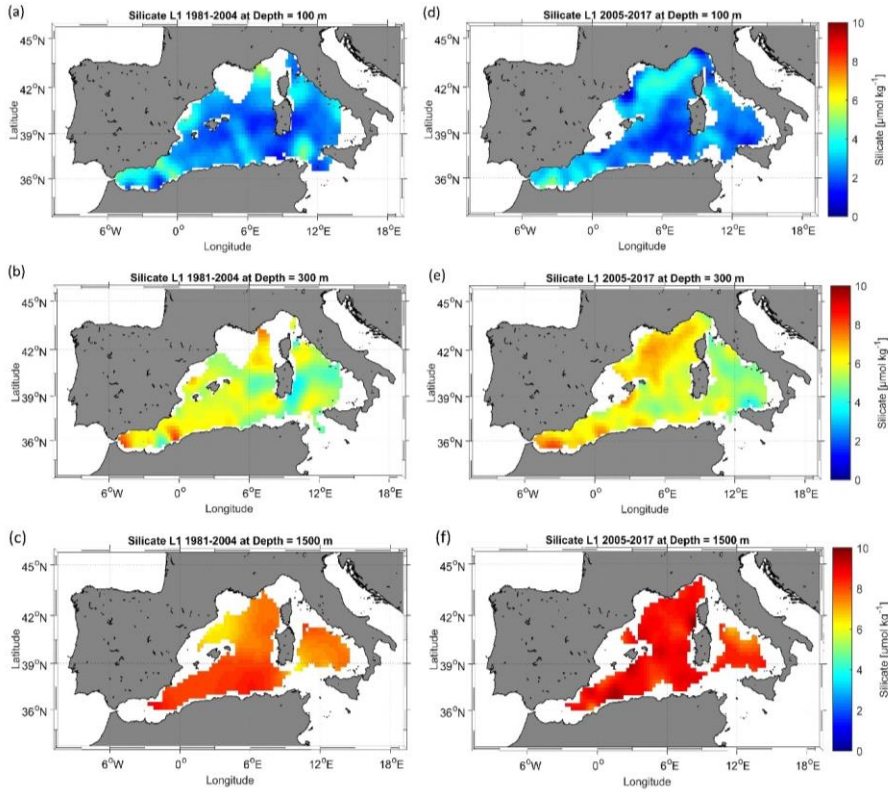
842

843 **Figure 20**Figure 19. The same as Fig. 18-19 but for phosphate.

844

**Formatted:** Font: Bold, Complex Script Font: Bold

**Formatted:** Font: Bold, Complex Script Font: Bold

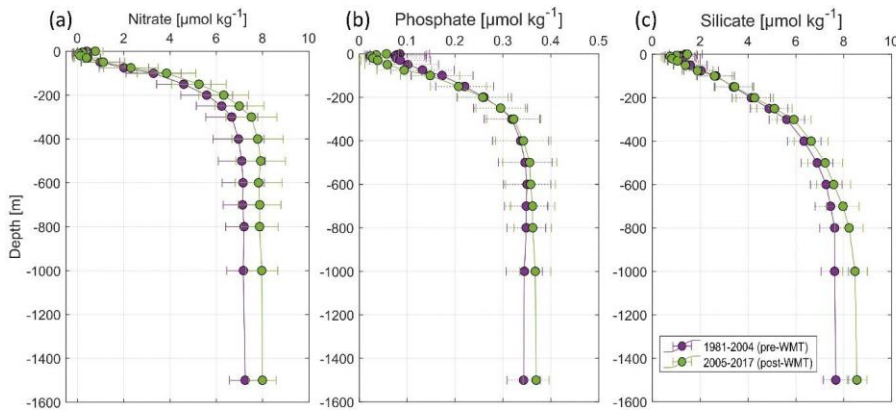


845

846 **Figure 21** ~~Figure 20~~. The same as Fig. 18-19 but for silicate.

**Formatted: Font: Bold, Complex Script Font: Bold**

**Formatted: Font: Bold, Complex Script Font: Bold**



847

848 ~~Figure 22, Figure 21.~~ Climatological mean vertical profile and standard deviation of (a) nitrate, (b)  
849 phosphate and (c) silicate over the WMED before (1981-2004, in violet) and after WMT (2005-2017,  
850 in green).

Formatted: Font: Bold, Complex Script Font: Bold

Formatted: Font: Bold, Complex Script Font: Bold

Formatted: Font: Bold, Complex Script Font: Bold

## 851 5 Data availability

852 The climatologies of Nitrate, Phosphate and Silicate ~~final product is~~ available as netCDF files from  
853 ~~the data repository~~ PANGAEA and can be accessed at  
854 ~~https://doi.pangaea.de/10.1594/PANGAEA.930447~~ <https://doi.org/10.1594/PANGAEA.930447>  
855 (Belgacem et al., 2021, ~~DOI registration in progress~~). Ancillary information is in the readme in  
856 PANGAEA with the list of variables that ~~is~~ are described in table 3 of section 4. ~~The MOOSE-GE data~~  
857 ~~are available in the SISMER database (global DOI 10.18142/235)~~

Formatted: Font: (Default) Times New Roman, Not Bold, Font color: Auto, Complex Script Font: Times New Roman, Not Bold

Formatted: Font: (Default) +Headings CS (Times New Roman), Complex Script Font: +Headings CS (Times New Roman)

Formatted: Font: (Default) +Headings CS (Times New Roman), Font color: Auto, Complex Script Font: +Headings CS (Times New Roman)

Formatted: Font: (Default) +Headings CS (Times New Roman), Complex Script Font: +Headings CS (Times New Roman)

Formatted: Font: (Default) +Headings CS (Times New Roman), Complex Script Font: +Headings CS (Times New Roman)

Formatted: Font: (Default) +Headings CS (Times New Roman), Complex Script Font: +Headings CS (Times New Roman)

## 858 6 Conclusion

859 In this study, we investigated spatial variability of the inorganic nutrients in the WMED and presented  
860 a climatological field reconstruction of nitrate, phosphate, and silicate, using an important collection  
861 dataset spanning 1981 and 2017. The BGC-WMED new product is generated on 19 vertical levels on a  
862  $1/4^\circ$  spatial resolution grid.

863 The new product represents ~~very well the~~ spatial patterns about nutrient distribution ~~very well~~ because  
864 of its higher spatial and temporal data coverage compared to the existing climatological products (see  
865 Table 1), it is contributing to the understanding of the spatial variability of nutrients in the WMED.

866 The novelty of the present work is the use of the variational analysis that takes into consideration  
867 physical, geographical boundaries and topography, the resulting estimate of ~~the~~ associated error field.

868 Comparison with previously reported studies gives that the BGC-WMED reproduces common features  
869 and agrees with previous records. The reference products WOA18 and medBFM biogeochemical  
870 reanalysis tend to underestimate nutrient distribution in the region with respect to the new product.

871 The new product captures the strong east-west gradient of and vertical features. The results obtained do  
872 not include seasonal or annual analysis fields. However, the aggregated dataset here does show  
873 improvements in describing the spatial distribution of inorganic nutrients in the WMED. We  
874 acknowledge that computing a climatological mean over a time period is not enough to estimate and  
875 detect the climate shift 'WMT' change driven trend. However, comparing climatologies based on the  
876 two time periods: 1981-2004 (pre-WMT) and 2005 -2017 (post-WMT) has already produced important  
877 results. Notable changes have been found in nutrient distribution after the WMT at various depths.

878 The results support the tendency to a relative increasing load of inorganic nutrients to the WMED and  
 879 possibly relate the change in general circulation patterns, changes in deep stratification and warming  
 880 trends, however, this remains to be evidenced.

881 The BGC-WMED is a regional climatology that has allowed the identification of a substantial  
 882 enrichment of the waters, except for the Tyrrhenian Sea where the water column is depleted in nutrients  
 883 with respect to the western areas of the WMED. The climatology gave information about the spreading  
 884 of inorganic nutrients inside the WMED at surface, intermediate and deep layers.

885 A future work will suggest a better understanding of the change in nutrients related to water masses  
 886 associated with ventilation rate, a climatological field along isopycnal surfaces instead of depths and the  
 887 correlation between potential temperature and nutrients.

888 **Appendix A: Additional information about cruise metadata**

889 **Table A1.** Summary table of the analytical techniques and instruments used for nutrient analysis.

Data source	Analytical methods	Reference
<a href="#">MEDATLAS</a>	-flow analysis system (autoanalyser) equipped with Chemlab -technicon colorimeters.	<a href="http://www.ifremer.fr/mater/dataset_i/c_hemitt.html">http://www.ifremer.fr/mater/dataset_i/c_hemitt.html</a>
<a href="#">SEADATANET including MOOSE-GE</a>	- flow analysis system (autoanalyser) equipped with Bran-Luebbe Seal	<a href="https://www.obs-banyuls.fr/fr/observer/moose.html">https://www.obs-banyuls.fr/fr/observer/moose.html</a>
<a href="#">CNR DIN WMED 20042017</a>	-continuous-flow system multichannel (Auto Analyzer Bran+Luebbe III Generation -OI-Analytical (Flow Solution III) flow-segmented -Systea discrete analyzer EasyChem Plus	Belgacem et al.,(2020) <a href="https://doi.org/10.5194/essd-12-1985-2020">https://doi.org/10.5194/essd-12-1985-2020</a>
<u>Other cruises:</u> <a href="#">Medship programs:</a> <a href="#">GLODAPv2;</a> <a href="#">CARIMED</a>	nutrient analysis strictly followed the recommendation of the World Ocean Circulation Experiment (WOCE) and the GO-SHIP protocols example: Quattro auto-analyzer from SEAL analytics.	Schroeder et al., (2015) Tanhua et al., (2013) <a href="https://doi.org/10.5194/essd-5-289-2013">https://doi.org/10.5194/essd-5-289-2013</a> Olsen et al., (2016) Hydes et al., (2010)

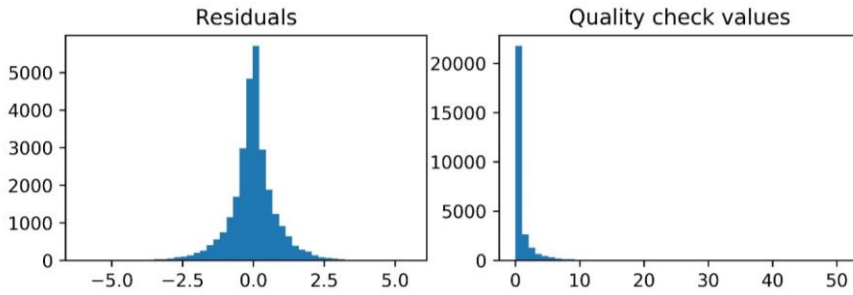
Formatted: English (United States)  
 Field Code Changed  
 Formatted: English (United States)  
 Formatted: English (United States)

890 **Appendix B: Additional information about quality assurance**

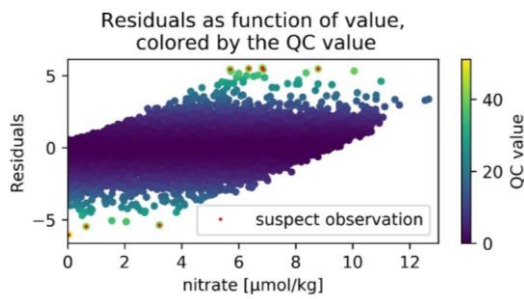
891 **Table A2.** Summary of the quality check analysis quality assurance of 1981-2017 climatology.

RMS	Nitrate	Phosphate	Silicate
Pre-quality check	0.848	0.05	0.763
<b>Post-quality check</b>	<b>0.838</b>	<b>0.049</b>	<b>0.757</b>
Number of suspected points	10	6	2

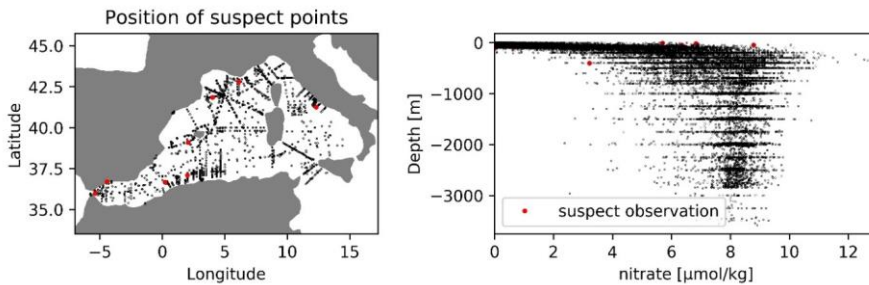
892



893  
 894 **Figure A1.** Overview of residual distribution and quality check values for Nitrate gridded fields (1981-2017)  
 895 before the quality check.



896  
 897 **Figure A2.** Scatterplot of residual as function of nitrate values (1981-2017) colored by the quality check values.  
 898 The red dots are the suspect observation (points with qcvalues > 40).



899  
 900 **Figure A3.** Position of the suspect points (nitrate climatology 1981-2017).

**Formatted:** Left  
**Formatted:** Font: (Default) +Headings CS (Times New Roman), 10 pt, Complex Script Font: +Headings CS (Times New Roman), 10 pt, English (United States)

901 **Appendix C: Additional information about temporal comparison**

902

903

904

905

906

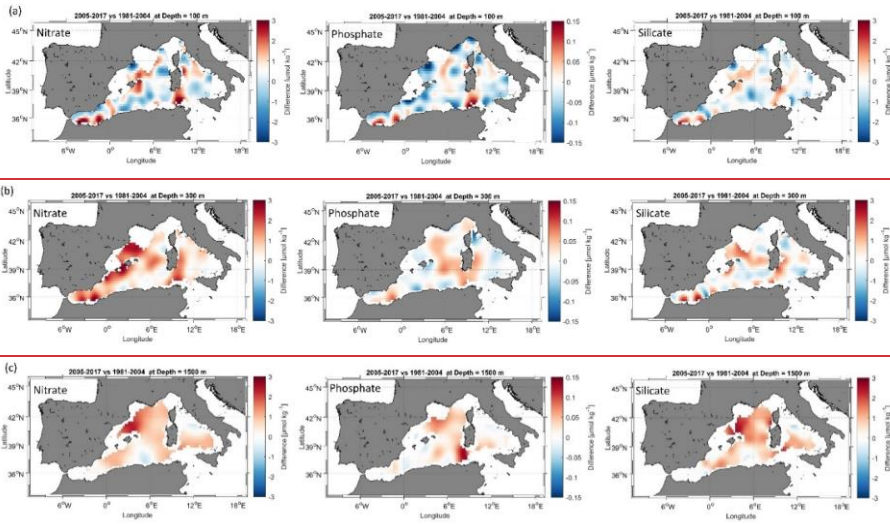


**Figure A4.** (a) Difference field at 100 m between the 1981-2004 climatology and the 2005-2017 climatologies; (b) Difference field at 300 m (c) Difference field at 1500 m.

907

908 **Author contributions**

909 The BGC-WMED climatology product was led between the CNR-ISMAR and DAIS- University of  
910 Venice. MB, KS and JC designed the experiment and contributed to the writing of the manuscript. AB  
911 and CT helped MB to perform the analysis and contributed to the manuscript. BP contributed to  
912 specific parts of the manuscript. PR and NG contributed to nutrient analyses during the last 10 years if  
913 the MOOSE cruises in the northern Mediterranean Sea.

914 **Acknowledgements**

915 Data was provided through SeaDataNet Pan-European infrastructure for ocean and marine data  
916 management (<https://www.seadatanet.org>), Mediterranean Ocean Observing System for the  
917 Environment, MOOSE (<http://www.moose-network.fr/>). thanks to the tremendous work of Patrick  
918 Raimbault and Nicole Garcia (MIO, Mediterranean Institute of Oceanography) during the last 10 years.  
919 MB acknowledge the WOA18 and CMEMS for the medBFM data ([https://help-cmems.mercator-](https://help-cmems.mercator-ocean.fr/en/articles/4444611-how-to-cite-or-reference-copernicus-marine-products-and-services)  
920 [ocean.fr/en/articles/4444611-how-to-cite-or-reference-copernicus-marine-products-and-services](https://help-cmems.mercator-ocean.fr/en/articles/4444611-how-to-cite-or-reference-copernicus-marine-products-and-services) ). We  
921 wish to thank all colleagues who contributed ~~in~~to the data acquisition, and the PIs of the cruises  
922 involved. MB thanks Kanwal Shahzadi from the university of Bologna for the discussions during our  
923 internship at GHER, ~~at~~University of Liège. We are grateful to the Institut National des Sciences de  
924 l'Univers (CNRS-INSU) and European projects for supporting the MOOSE network. JC and KS  
925 acknowledge several of national and European projects, e.g.: KM3NeT, EU GA #011937; SESAME,  
926 EU GA #GOCE-036949; PERSEUS, EU GA #287600; OCEAN-CERTAIN, EU GA #603773;  
927 COMMON SENSE, EU GA #228344; EUROFLEETS, EU GA #228344; EUROFLEETS2, EU GA #  
928 312762; JERICO, EU GA #262584; the Italian PRIN 2007 program “Tyrrhenian Seamounts  
929 ecosystems”, and the Italian RITMARE Flagship Project, both funded by the Italian Ministry of  
930 University and Research.

931

932 **References**

933 Barnes, S.L. (1964). A technique for maximizing details in numerical weather map analysis. J. App.  
934 Meteor., 3, 396-409.  
935 Barnes, S.L. (1994). Applications of the Barnes Objective Analysis Scheme, Part III: Tuning for  
936 Minimum Error. J. Atmosph. and Oceanic Tech., 11, 1459-1479.  
937 Barth, A., Troupin, C., Alvera-Azcárate, A. and Vandenbulcke, L.: Divand-1.0: N-dimensional  
938 variational data analysis for ocean observations, Geosci. Model Dev., 7(1), 225–241,  
939 doi:10.5194/gmd-7-225-2014, 2014.

**Formatted:** Font: (Default) Times New Roman, Font color: Auto, Complex Script Font: Times New Roman

**Formatted:** Font: (Default) Times New Roman, Font color: Auto, Complex Script Font: Times New Roman

**Formatted:** Font: (Default) Times New Roman, Font color: Auto, Complex Script Font: Times New Roman

**Formatted:** Font: (Default) Times New Roman, 11 pt, Font color: Auto, Complex Script Font: Times New Roman, 11 pt, Pattern: Clear

**Formatted:** Font: (Default) Times New Roman, 11 pt, Font color: Auto, Complex Script Font: Times New Roman, 11 pt, Pattern: Clear

**Formatted:** Font: (Default) Times New Roman, 11 pt, Font color: Auto, Complex Script Font: Times New Roman, 11 pt, Pattern: Clear

**Formatted:** Font: (Default) Times New Roman, 11 pt, Font color: Auto, Complex Script Font: Times New Roman, 11 pt, Pattern: Clear

**Formatted:** Font: (Default) Times New Roman, 11 pt, Font color: Auto, Complex Script Font: Times New Roman, 11 pt, Pattern: Clear

**Formatted:** Font: (Default) Times New Roman, Font color: Auto, Complex Script Font: Times New Roman, Pattern: Clear

940 Beckers, J. M., Barth, A., Troupin, C. and Alvera-Azcárate, A.: Approximate and efficient methods to  
941 assess error fields in spatial gridding with data interpolating variational analysis (DIVA), *J. Atmos.*  
942 *Ocean. Technol.*, 31(2), 515–530, doi:10.1175/JTECH-D-13-00130.1, 2014.

943 Belgacem, M., Chiggiato, J., Borghini, M., Pavoni, B., Cerrati, G., Acri, F., Cozzi, S., Ribotti, A.,  
944 Álvarez, M., Lauvset, S. K. and Schroeder, K.: Dissolved inorganic nutrients in the western  
945 Mediterranean Sea (2004–2017), *Earth Syst. Sci. Data*, 12(3), 1985–2011, doi:10.5194/essd-12-1985-  
946 2020, 2020.

947 Bethoux, J. P., Morin, P., Madec, C. and Gentili, B.: Phosphorus and nitrogen behaviour in the  
948 Mediterranean Sea, *Deep Sea Res. Part A, Oceanogr. Res. Pap.*, 39(9), 1641–1654, doi:10.1016/0198-  
949 0149(92)90053-V, 1992.

950 Brankart, J. M. and Brasseur, P.: The general circulation in the Mediterranean Sea: A climatological  
951 approach, *J. Mar. Syst.*, 18(1–3), 41–70, doi:10.1016/S0924-7963(98)00005-0, 1998.

952 Brasseur, P., Beckers, J. M., Brankart, J. M. and Schoenauen, R.: Seasonal temperature and salinity  
953 fields in the Mediterranean Sea: Climatological analyses of a historical data set, *Deep. Res. Part I*  
954 *Oceanogr. Res. Pap.*, 43(2), 159–192, doi:10.1016/0967-0637(96)00012-X, 1996.

955 Brasseur, P. P.: A variational inverse method for the reconstruction of general circulation fields in the  
956 northern Bering Sea, *J. Geophys. Res.*, 96(C3), 4891, doi:10.1029/90jc02387, 1991.

957 Buga, L., Eilola, K., Wesslander, K., Fryberg, L., Gatti, J., Leroy, D., Iona, S., Tsompanou, M. and  
958 Lipizer, M.: EMODnet Thematic Lot n ° 4 / SI2 . 749773 Interpolating Variational Analysis ( DIVA ).  
959 Release 2018, , doi:10.6092/A8CFB472-10DB-4225-9737-5A60DA9AF523, 2019.

960 Capet, A., Troupin, C., Carstensen, J., Grégoire, M. and Beckers, J. M.: Untangling spatial and  
961 temporal trends in the variability of the Black Sea Cold Intermediate Layer and mixed Layer Depth  
962 using the DIVA detrending procedure, *Ocean Dyn.*, 64(3), 315–324, doi:10.1007/s10236-013-0683-4,  
963 2014.

964 Van Cappellen, P., Powley, H. R., Emeis, K. C. and Krom, M. D.: A biogeochemical model for  
965 phosphorus and nitrogen cycling in the Eastern Mediterranean Sea: Part 1: Model development,  
966 initialization and sensitivity, *J. Mar. Syst.*, 139, 460–471, doi:10.1016/j.jmarsys.2014.08.016, 2014.

967 Crispi, G., Mosetti, R., Solidoro, C. and Crise, A.: Nutrients cycling in Mediterranean basins: The role  
968 of the biological pump in the trophic regime, in *Ecological Modelling*, vol. 138, pp. 101–114., 2001.

969 Crombet, Y., Leblanc, K., Quéuiner, B., Moutin, T., Rimmelin, P., Ras, J., Claustre, H., Leblond, N.,  
970 Oriol, L. and Pujo-Pay, M.: Deep silicon maxima in the stratified oligotrophic Mediterranean Sea,  
971 *Biogeosciences*, 8(2), 459–475, doi:10.5194/bg-8-459-2011, 2011.

972 D’Ortenzio, F. and Ribera d’Alcalà, M.: On the trophic regimes of the Mediterranean Sea: a satellite  
973 analysis, *Biogeosciences Discuss.*, 5(4), 2959–2983, doi:10.5194/bgd-5-2959-2008, 2009.

974 D’Ortenzio, F., Taillandier, V., Claustre, H., Prieur, L. M., Leymarie, E., Mignot, A., Poteau, A.,  
975 Penker, C. and Schmechtig, C. M.: Biogeochemical Argo : The Test Case of the NAOS  
976 Mediterranean Array, , 7(March), 1–16, doi:10.3389/fmars.2020.00120, 2020.

977 DeMaster, D. J.: The accumulation and cycling of biogenic silica in the Southern Ocean: Revisiting  
978 the marine silica budget, *Deep. Res. Part II Top. Stud. Oceanogr.*, 49(16), 3155–3167,  
979 doi:10.1016/S0967-0645(02)00076-0, 2002.

980 Desroziers, G., Berre, L., Chapnik, B. and Poli, P.: Diagnosis of observation, background and  
981 analysis-error statistics in observation space, *Q. J. R. Meteorol. Soc.*, 131(613), 3385–3396,  
982 doi:10.1256/qj.05.108, 2005.

983 Diaz, P., Raimbault, F., Boudjellal, B., Garcia, N. and Moutin, T.: Early spring phosphorus limitation  
984 of primary productivity in a NW Mediterranean coastal zone (Gulf of Lions), *Mar. Ecol. Prog. Ser.*,  
985 211(McGill 1965), 51–62, doi:10.3354/meps211051, 2001.



986 Fichaut, M., Garcia, M. J., Giorgetti, A., Iona, A., Kuznetsov, A., Rixen, M. and Group, M.:  
987 MEDAR/MEDATLAS 2002: A Mediterranean and Black Sea database for operational oceanography,  
988 Elsevier Oceanogr. Ser., 69(C), 645–648, doi:10.1016/S0422-9894(03)80107-1, 2003.

989 de Fommervault, O. P., Migon, C., D’Ortenzio, F., Ribera d’Alcalà, M. and Coppola, L.: Temporal  
990 variability of nutrient concentrations in the northwestern Mediterranean sea (DYFAMED time-series  
991 station), Deep. Res. Part I Oceanogr. Res. Pap., 100, 1–12, doi:10.1016/j.dsr.2015.02.006, 2015.

992 Frings, P. J., Clymans, W., Fontorbe, G., De La Rocha, C. L. and Conley, D. J.: The continental Si  
993 cycle and its impact on the ocean Si isotope budget, Chem. Geol., 425, 12–36,  
994 doi:10.1016/j.chemgeo.2016.01.020, 2016.

995 García-Martínez, M. del C., Vargas-Yáñez, M., Moya, F., Santiago, R., Muñoz, M., Reul, A.,  
996 Ramírez, T. and Balbín, R.: Average nutrient and chlorophyll distributions in the western  
997 Mediterranean: RADMED project, Oceanologia, 61(1), 143–169, doi:10.1016/j.oceano.2018.08.003,  
998 2019.

999 Garcia, H. E., Weathers, K. W., Paver, C. R., Smolyar, I., Boyer, T. P., Locarnini, R. A., Zweng, M.  
1000 M., Mishonov, A. V., Baranova, O. K., Seidov, D. and Reagan, J. R.: World Ocean Atlas 2018. Vol. 4:  
1001 Dissolved Inorganic Nutrients (phosphate, nitrate and nitrate+nitrite, silicate), 2019.

1002 Giorgi, F.: Climate change hot-spots, Geophys. Res. Lett., 33(8), 1–4, doi:10.1029/2006GL025734,  
1003 2006.

1004 Hecht, A., Pinardi, N. and Robinson, A. R.: Currents, Water Masses, Eddies and Jets in the  
1005 Mediterranean Levantine Basin, J. Phys. Oceanogr., 18(10), 1320–1353, 1988.

1006 Houpert, L., Durrieu de Madron, X., Testor, P., Bosse, A., D’Ortenzio, F., Bouin, M. N., Dausse, D.,  
1007 Le Goff, H., Kunesch, S., Labaste, M., Coppola, L., Mortier, L. and Raimbault, P.: Observations of  
1008 open-ocean deep convection in the northwestern Mediterranean Sea: Seasonal and interannual  
1009 variability of mixing and deep water masses for the 2007–2013 Period, J. Geophys. Res. Ocean.,  
1010 121(11), 8139–8171, doi:10.1002/2016JC011857, 2016.

1011 Key, R. M., Kozyr, A., Sabine, C. L., Lee, K., Wanninkhof, R., Bullister, J. L., Feely, R. A., Millero,  
1012 F. J., Mordy, C. and Peng, T. H.: A global ocean carbon climatology: Results from Global Data  
1013 Analysis Project (GLODAP), Global Biogeochem. Cycles, 18(4), 1–23, doi:10.1029/2004GB002247,  
1014 2004.

1015 Krom, M. D., Oceanographic, I. and Shikmona, T.: Nutrient budget for the Eastern Mediterranean :  
1016 Implications for phosphorus limitation, , 49(5), 1582–1592, 2004.

1017 Krom, M. D., Emeis, K. C. and Van Cappellen, P.: Why is the Eastern Mediterranean phosphorus  
1018 limited?, Prog. Oceanogr., 85(3–4), 236–244, doi:10.1016/j.pocean.2010.03.003, 2010.

1019 Krom, M. D., Kress, N. and Fanning, K.: Silica cycling in the ultra-oligotrophic eastern Mediterranean  
1020 Sea, Biogeosciences, 11(15), 4211–4223, doi:10.5194/bg-11-4211-2014, 2014.

1021 Lascaratos, A., Roether, W. and Nittis, K.: Recent changes in deep water formation and spreading in  
1022 the eastern Mediterranean Sea : a review, , 44, 5–36, 1999.

1023 Lauvset, S. K., Key, R. M., Olsen, A., Van Heuven, S., Velo, A., Lin, X., Schirnick, C., Kozyr, A.,  
1024 Tanhua, T., Hoppema, M., Jutterström, S., Steinfeldt, R., Jeansson, E., Ishii, M., Perez, F. F., Suzuki,  
1025 T. and Watelet, S.: A new global interior ocean mapped climatology: The  $1^\circ \times 1^\circ$  GLODAP version 2,  
1026 Earth Syst. Sci. Data, 8(2), 325–340, doi:10.5194/essd-8-325-2016, 2016.

1027 Lavigne, H.: On the vertical distribution of the chlorophyll a concentration in the Mediterranean Sea :  
1028 a basin scale and seasonal approach, , (March), doi:10.5194/bgd-12-4139-2015, 2015.

1029 Lazzari, P., Solidoro, C., Ibello, V., Salon, S., Teruzzi, A., Béranger, K., Colella, S. and Crise, A.:  
1030 Seasonal and inter-annual variability of plankton chlorophyll and primary production in the  
1031 Mediterranean Sea: A modelling approach, Biogeosciences, 9(1), 217–233, doi:10.5194/bg-9-217-

- 1032 2012, 2012.
- 1033 Lazzari, P., Solidoro, C., Salon, S. and Bolzon, G.: Spatial variability of phosphate and nitrate in the  
1034 Mediterranean Sea: A modeling approach, *Deep. Res. Part I Oceanogr. Res. Pap.*, 108, 39–52,  
1035 doi:10.1016/j.dsr.2015.12.006, 2016.
- 1036 Levitus, S.: Climatological Atlas of the World Ocean, *Eos, Trans. Am. Geophys. Union*, 64(49), 962–  
1037 963, doi:10.1029/EO064i049p00962-02, 1982.
- 1038 Li, P. and Tanhua, T.: Recent Changes in Deep Ventilation of the Mediterranean Sea; Evidence From  
1039 Long-Term Transient Tracer Observations, *Front. Mar. Sci.*, 7(July), 1–23,  
1040 doi:10.3389/fmars.2020.00594, 2020.
- 1041 Lipizer, M., Partescano, E., Rabitti, A., Giorgetti, A. and Crise, A.: Qualified temperature, salinity and  
1042 dissolved oxygen climatologies in a changing Adriatic Sea, *Ocean Sci.*, 10(5), 771–797,  
1043 doi:10.5194/os-10-771-2014, 2014.
- 1044 Lucea, A., Duarte, C. M. and Agustí, S.: Nutrient ( N , P and Si ) and carbon partitioning in the  
1045 stratified NW Mediterranean, , 49, 157–170, doi:10.1016/S1385-1101(03)00005-4, 2003.
- 1046 Ludwig, W., Dumont, E., Meybeck, M. and Heussner, S.: River discharges of water and nutrients to  
1047 the Mediterranean and Black Sea: Major drivers for ecosystem changes during past and future  
1048 decades?, *Prog. Oceanogr.*, 80(3–4), 199–217, doi:10.1016/j.pocean.2009.02.001, 2009.
- 1049 Ludwig, W., Bouwman, A. F., Dumont, E. and Lespinas, F.: Water and nutrient fluxes from major  
1050 Mediterranean and Black Sea rivers: Past and future trends and their implications for the basin-scale  
1051 budgets, *Global Biogeochem. Cycles*, 24(4), 1–14, doi:10.1029/2009GB003594, 2010.
- 1052 Maillard, C., Lowry, R., Maudire, G. and Schaap, D.: SeaDataNet: Development of a Pan-European  
1053 infrastructure for ocean and marine data management, in *OCEANS 2007 - Europe.*, 2007.
- 1054 Malanotte-Rizzoli, P., Manca, B. B., D’Alcala, M. R., Theocharis, A., Brenner, S., Budillon, G. and  
1055 Ozsoy, E.: The Eastern Mediterranean in the 80s and in the 90s: The big transition in the intermediate  
1056 and deep circulations, *Dyn. Atmos. Ocean.*, 29(2–4), 365–395, doi:10.1016/S0377-0265(99)00011-1,  
1057 1999.
- 1058 Manca, B., Burca, M., Giorgetti, A., Coatanoean, C., Garcia, M. J. and Iona, A.: Physical and  
1059 biochemical averaged vertical profiles in the Mediterranean regions: An important tool to trace the  
1060 climatology of water masses and to validate incoming data from operational oceanography, *J. Mar.  
1061 Syst.*, 48(1–4), 83–116, doi:10.1016/j.jmarsys.2003.11.025, 2004.
- 1062 Míguez, B. M., Novellino, A., Vinci, M., Claus, S., Calewaert, J. B., Vallius, H., Schmitt, T., Pititto,  
1063 A., Giorgetti, A., Askew, N., Iona, S., Schaap, D., Pinardi, N., Harpham, Q., Kater, B. J., Populus, J.,  
1064 She, J., Palazov, A. V., McMeel, O., Oset, P., Lear, D., Manzella, G. M. R., Gorringer, P., Simoncelli,  
1065 S., Larkin, K., Holdsworth, N., Arvanitidis, C. D., Jack, M. E. M., Chaves Montero, M. del M.,  
1066 Herman, P. M. J. and Hernandez, F.: The European Marine Observation and Data Network  
1067 (EMODnet): Visions and roles of the gateway to marine data in Europe, *Front. Mar. Sci.*, 6(JUL), 1–  
1068 24, doi:10.3389/fmars.2019.00313, 2019.
- 1069 Moon, J., Lee, K., Tanhua, T., Kress, N. and Kim, I.: Temporal nutrient dynamics in the  
1070 Mediterranean Sea in response to anthropogenic inputs, , 5243–5251,  
1071 doi:10.1002/2016GL068788.Received, 2016.
- 1072 Moore, C. M., Mills, M. M., Arrigo, K. R., Berman-Frank, I., Bopp, L., Boyd, P. W., Galbraith, E. D.,  
1073 Geider, R. J., Guieu, C., Jaccard, S. L., Jickells, T. D., La Roche, J., Lenton, T. M., Mahowald, N. M.,  
1074 Marañón, E., Marinov, I., Moore, J. K., Nakatsuka, T., Oschlies, A., Saito, M. A., Thingstad, T. F.,  
1075 Tsuda, A. and Ulloa, O.: Processes and patterns of oceanic nutrient limitation, *Nat. Geosci.*, 6(9), 701–  
1076 710, doi:10.1038/ngeo1765, 2013.
- 1077 Murphy, A. H.: Skill Scores Based on the Mean Square Error and Their Relationships to the  
1078 Correlation Coefficient, *Mon. Weather Rev.*, 116(12), 2417–2424, doi:10.1175/1520-

1079 0493(1988)116<2417:SSBOTM>2.0.CO;2, 1988.

1080 Ozer, T., Gertman, I., Kress, N., Silverman, J. and Herut, B.: Interannual thermohaline (1979–2014)  
1081 and nutrient (2002–2014) dynamics in the Levantine surface and intermediate water masses, SE  
1082 Mediterranean Sea, *Glob. Planet. Change*, doi:10.1016/j.gloplacha.2016.04.001, 2017.

1083 Piñeiro, S., González-Pola, C., Fernández-Díaz, J. M. and Balbin, R.: Thermohaline Evolution of the  
1084 Western Mediterranean Deep Waters Since 2005: Diffusive Stages and Interannual Renewal  
1085 Injections, *J. Geophys. Res. Ocean.*, 124(12), 8747–8766, doi:10.1029/2019JC015094, 2019.

1086 Pondaven, P., Ruiz-Pino, D., Druon, J. N., Fravalo, C. and Tréguer, P.: Factors controlling silicon and  
1087 nitrogen biogeochemical cycles in high nutrient, low chlorophyll systems (the Southern Ocean and the  
1088 North Pacific): Comparison with a mesotrophic system (the North Atlantic), *Deep. Res. Part I*  
1089 *Oceanogr. Res. Pap.*, 46(11), 1923–1968, doi:10.1016/S0967-0637(99)00033-3, 1999.

1090 Pujo-Pay, M., Conan, P., Oriol, L., Cornet-Barthaux, V., Falco, C., Ghiglione, J. F., Goyet, C.,  
1091 Moutin, T. and Prieur, L.: Integrated survey of elemental stoichiometry (C, N, P) from the western to  
1092 eastern Mediterranean Sea, *Biogeosciences*, 8(4), 883–899, doi:10.5194/bg-8-883-2011, 2011.

1093 Rahav, E., Herut, B., Stambler, N., Bar-Zeev, E., Mulholland, M. R. and Berman-Frank, I.:  
1094 Uncoupling between dinitrogen fixation and primary productivity in the eastern Mediterranean Sea, *J.*  
1095 *Geophys. Res. Biogeosciences*, 118(1), 195–202, doi:10.1002/jgrg.20023, 2013.

1096 Reale, M., Giorgi, F., Solidoro, C., Di Biagio, V., Di Sante, F., Mariotti, L., Farneti, R. and Sannino,  
1097 G.: The Regional Earth System Model RegCM-ES: Evaluation of the Mediterranean climate and  
1098 marine biogeochemistry., 2020.

1099 Reul, A., Rodríguez, V., Jiménez-Gómez, F., Blanco, J. M., Bautista, B., Sarhan, T., Guerrero, F.,  
1100 Ruiz, J. and García-Lafuente, J.: Variability in the spatio-temporal distribution and size-structure of  
1101 phytoplankton across an upwelling area in the NW-Alboran Sea, (W-Mediterranean), *Cont. Shelf Res.*,  
1102 25(5–6), 589–608, doi:10.1016/j.csr.2004.09.016, 2005.

1103 Ribera d'Alcalà, M.: Nutrient ratios and fluxes hint at overlooked processes in the Mediterranean Sea,  
1104 *J. Geophys. Res.*, 108(C9), doi:10.1029/2002jc001650, 2003.

1105 Ribera d'Alcalà, M., Civitarese, G., Conversano, F. and Lavezza, R.: Nutrient ratios and fluxes hint at  
1106 overlooked processes in the Mediterranean Sea, *J. Geophys. Res. Ocean.*, 108(9),  
1107 doi:10.1029/2002jc001650, 2003.

1108 Rixen, M., Beckers, J. M., Brankart, J. M. and Brasseur, P.: A numerically efficient data analysis  
1109 method with error map generation, *Ocean Model.*, 2(1–2), 45–60, doi:10.1016/s1463-5003(00)00009-  
1110 3, 2000.

1111 Roether, W. and Schlitzer, R.: Eastern Mediterranean deep water renewal on the basis of  
1112 chlorofluoromethane and tritium data, *Dyn. Atmos. Ocean.*, 15(3–5), 333–354, doi:10.1016/0377-  
1113 0265(91)90025-B, 1991.

1114 Roether, W., Manca, Beniamino B. Klein, B., Bregant, D., Georgopoulos, D., Beitzel, V. and  
1115 KovaEevic, Vedrala Luchetta, A.: Recent Changes in Eastern Mediterranean Deep Waters., 1996.

1116 Roether, W., Klein, B., Bruno, B., Theocharis, A. and Kioroglou, S.: Progress in Oceanography  
1117 Transient Eastern Mediterranean deep waters in response to the massive dense-water output of the  
1118 Aegean Sea in the 1990s, , 74, 540–571, doi:10.1016/j.pocean.2007.03.001, 2007.

1119 Roether, W., Klein, B. and Hainbucher, D.: The Eastern Mediterranean Transient: Evidence for  
1120 Similar Events Previously?, *Mediterr. Sea Temporal Var. Spat. Patterns*, 9781118847(January), 75–  
1121 83, doi:10.1002/9781118847572.ch6, 2014.

1122 Salgado-Hernanz, P. M., Racault, M. F., Font-Muñoz, J. S. and Basterretxea, G.: Trends in  
1123 phytoplankton phenology in the Mediterranean Sea based on ocean-colour remote sensing, *Remote*  
1124 *Sens. Environ.*, 221(October 2018), 50–64, doi:10.1016/j.rse.2018.10.036, 2019.

- 1125 Sarmiento, J. L. and Toggweiler, J. R.: A new model for the role of the oceans in determining  
1126 atmospheric PCO<sub>2</sub>, *Nature*, 308(5960), 621–624, doi:10.1038/308621a0, 1984.
- 1127 Schröder, K., Gasparini, G. P., Tangherlini, M. and Astraldi, M.: Deep and intermediate water in the  
1128 western Mediterranean under the influence of the Eastern Mediterranean Transient, *Geophys. Res.  
1129 Lett.*, 33(21), 2–7, doi:10.1029/2006GL027121, 2006.
- 1130 Schroeder, K., Gasparini, G. P., Borghini, M., Cerrati, G. and Delfanti, R.: Biogeochemical tracers and  
1131 fluxes in the Western Mediterranean Sea, spring 2005, *J. Mar. Syst.*, 80(1–2), 8–24,  
1132 doi:10.1016/j.jmarsys.2009.08.002, 2010.
- 1133 Schroeder, K., Tanhua, T., Bryden, H., Alvarez, M., Chiggiato, J. and Aracri, S.: Mediterranean Sea  
1134 Ship-based Hydrographic Investigations Program (Med-SHIP), *Oceanography*, 28(3), 12–15,  
1135 doi:10.5670/oceanog.2015.71, 2015.
- 1136 Schroeder, K., Chiggiato, J., Bryden, H. L., Borghini, M. and Ismail, S. Ben: Abrupt climate shift in  
1137 the Western Mediterranean Sea, *Nat. Publ. Gr.*, 1–7, doi:10.1038/srep23009, 2016.
- 1138 Schroeder, K., Chiggiato, J., Josey, S. A., Borghini, M., Aracri, S. and Sparnocchia, S.: Rapid  
1139 response to climate change in a marginal sea, (May), 1–7, doi:10.1038/s41598-017-04455-5, 2017.
- 1140 Schroeder, K., Cozzi, S., Belgacem, M., Borghini, M., Cantoni, C., Durante, S., Petrizzo, A., Poiana,  
1141 A. and Chiggiato, J.: Along-Path Evolution of Biogeochemical and Carbonate System Properties in the  
1142 Intermediate Water of the Western Mediterranean, *Front. Mar. Sci.*, 7(May), 1–19,  
1143 doi:10.3389/fmars.2020.00375, 2020.
- 1144 Shepherd, J. G., Brewer, P. G., Oschlies, A. and Watson, A. J.: Ocean ventilation and deoxygenation  
1145 in a warming world: posters, *Philos. Trans. R. Soc. A Math. Phys. Eng. Sci.*, 375(2102), 20170241,  
1146 doi:10.1098/rsta.2017.0241, 2017.
- 1147 Sospedra, J., Niencheski, L. F. H., Falco, S., Andrade, C. F. F., Attisano, K. K. and Rodilla, M.:  
1148 ScienceDirect Identifying the main sources of silicate in coastal waters of the Southern Gulf of  
1149 Valencia ( Western Mediterranean Sea ), *Oceanologia*, 60(1), 52–64,  
1150 doi:10.1016/j.oceano.2017.07.004, 2018.
- 1151 Stöven, T. and Tanhua, T.: Ventilation of the mediterranean sea constrained by multiple transient  
1152 tracer measurements, *Ocean Sci.*, 10(3), 439–457, doi:10.5194/os-10-439-2014, 2014.
- 1153 Tanhua, T., Hainbucher, D., Schroeder, K., Cardin, V., Álvarez, M. and Civitarese, G.: The  
1154 Mediterranean Sea system: A review and an introduction to the special issue, *Ocean Sci.*, 9(5), 789–  
1155 803, doi:10.5194/os-9-789-2013, 2013.
- 1156 Testor, P., Bosse, A., Houpert, L., Margirier, F., Mortier, L., Legoff, H., Dausse, D., Labaste, M.,  
1157 Karstensen, J., Hayes, D., Olita, A., Ribotti, A., Schroeder, K., Chiggiato, J., Onken, R., Heslop, E.,  
1158 Mourre, B., D’ortenzio, F., Mayot, N., Lavigne, H., de Fommervault, O., Coppola, L., Prieur, L.,  
1159 Taillandier, V., Durrieu de Madron, X., Bourrin, F., Many, G., Damien, P., Estournel, C., Marsaleix,  
1160 P., Taupier-Letage, I., Raimbault, P., Waldman, R., Bouin, M. N., Giordani, H., Caniaux, G., Somot,  
1161 S., Ducrocq, V. and Conan, P.: Multiscale Observations of Deep Convection in the Northwestern  
1162 Mediterranean Sea During Winter 2012–2013 Using Multiple Platforms, *J. Geophys. Res. Ocean.*,  
1163 123(3), 1745–1776, doi:10.1002/2016JC012671, 2018.
- 1164 Theocharis, A., Lascaratos, A. and Sofianos, S.: Variability of sea water properties in the Ionian ,  
1165 Cretan and Levantine seas during the last century, (April), 22–24, 2002.
- 1166 Troupin, C., MacHín, F., Ouberdous, M., Sirjacobs, D., Barth, A. and Beckers, J. M.: High-resolution  
1167 climatology of the northeast Atlantic using Data-Interpolating Variational Analysis (Diva), *J.  
1168 Geophys. Res. Ocean.*, 115(8), 1–20, doi:10.1029/2009JC005512, 2010.
- 1169 Troupin, C., Barth, A., Sirjacobs, D., Ouberdous, M., Brankart, J. M., Brasseur, P., Rixen, M., Alvera-  
1170 Azcárate, A., Belounis, M., Capet, A., Lenartz, F., Toussaint, M. E. and Beckers, J. M.: Generation of  
1171 analysis and consistent error fields using the Data Interpolating Variational Analysis (DIVA), *Ocean*

- 1172 Model., 52–53, 90–101, doi:10.1016/j.ocemod.2012.05.002, 2012.
- 1173 Troupin, C., Watelet, S., Ouberdous, M., Sirjacobs, D., Barth, A., Toussaint, M. and Beckers, J.: Data  
1174 Interpolating Variational Analysis User Guide, , 836723, doi:10.5281/zenodo.836723, 2018.
- 1175 Vargas-yáñez, M.: Updating temperature and salinity mean values and trends in the Western  
1176 Mediterranean : The RADMED project Progress in Oceanography Updating temperature and salinity  
1177 mean values and trends in the Western Mediterranean : The RADMED project, Prog. Oceanogr.,  
1178 157(September), 27–46, doi:10.1016/j.pocean.2017.09.004, 2017.
- 1179 Weatherall, P., Marks, K. M., Jakobsson, M., Schmitt, T., Tani, S., Arndt, J. E., Rovere, M., Chayes,  
1180 D., Ferrini, V. and Wigley, R.: A new digital bathymetric model of the world's oceans, Earth Sp. Sci.,  
1181 2, 331–345, doi:doi: 10.1002/ 2015EA000107, 2015.
- 1182 Williams, R. G. and Follows, M. J.: Physical Transport of Nutrients and the Maintenance of Biological  
1183 Production, in Ocean Biogeochemistry, pp. 19–51., 2003.
- 1184